UNIVERSITY OF CALIFORNIA IRVINE

Nonlinear Microscopy through Surface Plasmon Polaritons

THESIS

submitted in partial satisfaction of the requirements

for the degree of

Master of Science

in Chemical and Materials Physics

by

John Kenison

THESIS COMMITTEE:

PROFESSOR ERIC O. POTMA, CHAIR

PROFESSOR MICHELLE DIGMAN

PROFESSOR WILSON HO

2018

Contents

List of Figures

ABSTRACT OF THE THESIS

Nonlinear Microscopy through Surface Plasmon Polaritons

by John Kenison

Master of Science, Physics

University of California Irvine, 2018

Professor Eric Potma, Chair

Surface plasmon polariton (SPP) modes on metallic films give rise to surface fields that can be used to enhance optical phenomena. Whereas SPP modes have been used to enhance the fluorescence and Raman response from molecules in the vicinity of the metallic surface, here we explore the use of SPP modes for detecting particles and structures that are non-fluorescent. In particular, we study the role of thin gold films in supporting SPP fields, which subsequently become distorted and confined by the presence of sub-μm-sized particles, resulting in nonlinear electron-hole pair generation in the gold followed by radiative recombination. This mechanism, in which the gold film is both the source of strong near-fields as well as the antenna for coupling radiation to the far-field, holds promise as a label-free sensing mechanism of small particles near the surface. In this work, the sensitivity and utility of this relatively unexplored property of thin gold films is investigated.

Chapter 1

Introduction

1.1 Label-free optical sensing

The success of optical sensing methods is due to the relatively efficient and non-destructive interaction between the sample and light field. The broad application of optical biosensors highlights the usefulness of optical probing methods. In many cases, sensing is achieved at surfaces, where changes near the sensor surface are translated in to an optical signal. In the case of fluorescence detection, nanoscopic fluorophores are excited and their emission is collected with a sensitive camera, thus enabling visualization of the emission event. The spatial resolution that can be achieved is then only limited by the ability to localize the emission source with a well characterized point spread function. Optical sensors based on fluorescence have impacted fluorescence-activated cell sorting, DNA sequencing, clinical diagnostics and many other fields. For other applications, however, fluorescent labeling

is not always an option. Phototoxicity, photobleaching or the lack of a suitable fluorescent probe can limit the utility of the fluorescence method. In this regard, optical sensing based on purely refractive properties of the sample is an attractive alternative. Since every sample exhibits intrinsic refractive optical properties, refractive sensing can simplify or sometimes avoid labeling protocols altogether, offering a simple yet powerful sensing approach.

High sensitivity levels have been achieved by monitoring phase or amplitude changes in an applied optical field due to differences in refractive index between the analyte and its environment. Integrated Mach-Zehnder and Young interferometers are examples of such refractometric sensing devices.(Heideman and Lambeck, 1999; Schmitt et al., 1997; Schmitt et al., 2007) The phase change introduced by a single particle, such as a liposome or virus, is sufficient to produce a detectable interferometric signal.(Kukura et al., 2009; Ortega-Arroyo and Kukura, 2012) Using an imaging approach, called interferometric scattering (iSCAT) microscopy, it has been shown that a single protein in solution can be detected based on the minuscule refractive changes it introduces when present in the detection window.(Ortega Arroyo et al., 2014)

Interferometric sensors have a wide range of applications, but their utility is ultimately limited by a detectable interference against a large background of the light field. An alternative strategy is the surface plasmon resonance (SPR) sensor, a refractometer that senses minute changes in the refractive index by monitoring variations in the coupling angle of a propagating light field to a surface plasmon polariton wave supported by a metal film.(Homola, 2008; Matsubara, Kawata, and

Minami, 1988; Zhang and Uttamchandani, 1988) This class of refractive sensors benefits from the unique properties of surface plasmon waves at metal-dielectric interfaces, which display exquisite sensitivity to small refractive changes in the immediate vicinity of the interface. SPR sensors do not require interferometric stability, which makes this approach robust and relatively simple. The fact that the technology has been commercialized by several manufacturers, including GE Healthcare Life Sciences (Biacore), Pioneer and Conductive Technologies, is testament to the reliability of the SPR approach. SPR biosensors have been used in a wide area of applications,(Homola, 2008; Boozer et al., 2006; Phillips and Cheng, 2007; Homola, Yee, and Gauglitz, 1999), ranging from detection of pathogens, toxins, pesticides, drugs, allergy markers, cancer markers, antibodies and more. As such, SPR based technologies have impacted the fields of medical diagnostics, food safety and environmental monitoring.

1.2 Surface Plasmon Polaritons

Surface plasmon polaritons result from a light-matter interaction, coupling collective electron oscillations near a metal surface to a propagating electromagnetic wave in an adjacent dielectric medium. Upon coupling freely propagating radiation to the SPP mode, the incident radiation is converted to an elliptically polarized plane wave that decays exponentially away from the metal/dielectric interface ($\sim$200nm).

The utility of evanescent fields as a probe field for biology at surfaces has been realized with total internal reflection fluorescence (TIRF) microscopy, where the supporting surface of relevance is formed by the glass/water interface. Imaging of cell membranes adhered to a glass coverslip was achieved over a wide field of view by exciting fluorescent labels and avoiding out of focus contributions from the sample bulk (Axelrod, 1981). For instance, direct measurements of single fluorescently labeled myosin molecules were accomplished in solution at video rates.

While geometrically similar to a TIRF microscope configuration, the addition of an SPP supporting gold film produces additional enhancement of the evanescent fields. For uniform layered planar media, this requires precise momentum matching between the in-plane component of a p-polarized light field and the associated out of plane electron oscillation of the same energy.

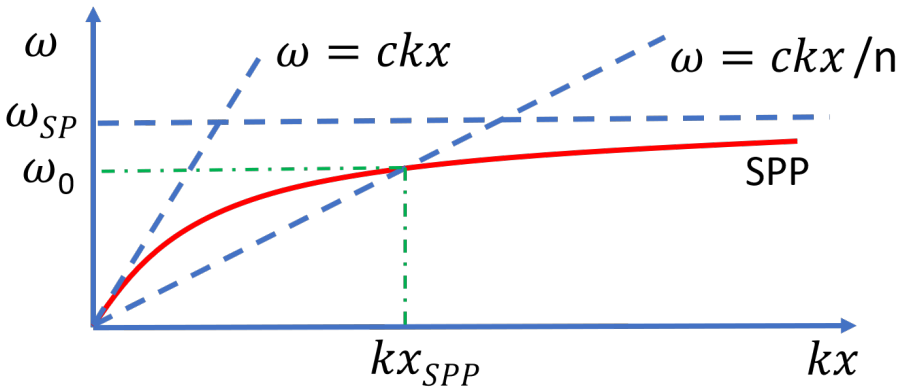

FIGURE 1.1: SPP dispersion curve

For a given frequency, a freely propagating beam has insufficient momenta to excite

an SPP. A strategy for overcoming this obstacle is to use the evanescent field generated beyond the critical angle at a planar interface as a driving field. The in-plane component of the evanescent field is greater than the corresponding propagating beam in the second half space, and is capable of driving SPP's at a near-by interface(Green et al., 2000; Zayats, Smolyaninov, and Maradudin, 2005). This mechanism is employed in Kretschmann and Otto configurations.

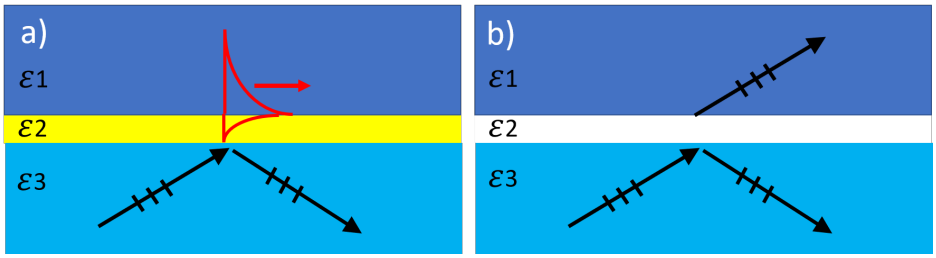

FIGURE 1.2: Three layered system. From bottom to top, the layers are glass/gold/air

In the case of a Kretschmann configuration, we can imagine a three layer system. A thin gold film is sandwiched by a glass layer in the form of a prism or objective lens along with an opposing dielectric halfspace, typically water. Solutions to Maxwells equations in the illuminated area of the film must satisfy boundary conditions at two closely spaced interfaces of the film with the surrounding environment. Beyond the critical angle for a glass-gold interface, the resulting evanescent field can have sufficient momenta along the interface to support SPP oscillations in the gold-dielectric boundary. When the incident beam is tuned to the Kretschmann angle, a noticeable decrease in the reflectance of the illuminated gold film is observed as energy is coupled into SPP modes.

Surface plasmon polaritons also have the ability to redirect near-field radiation to the far-field. The ability for an evanescent wave to couple to freely propagating modes is not unfamiliar even without the presence of plasmonic effects. Replacement of the gold film with an air gap allows for frustrated total internal reflection where evanescent fields at the 2-3 interface penetrate the 1-2 interface and emerge as freely propagating waves in medium 1. This optical tunneling effect forms the basis for leakage radiation (Hohenau et al., 2011), where evanescent fields associated with SPP waves extend into and through the metal side of the interface. This provides a far-field radiative channel for SPP waves propagating on a metallic film thin enough to allow an optical tunneling effect to occur. In the bottom half space, a freely propagating wave at the Kretschmann angle emerges and can be collected by a high NA objective. Surface plasmon coupled emission microscopy (SPCEM) relies on the coupling of the large momenta of evanescent fields from excited fluorophores near the metallic interface to propagating SPP modes. The resulting SPP fields radiate symmetrically on the gold film, emitting leakage radiation as they travel outward from the source. This illustrates the ability of a thin gold film to not only support an SPP excitation field but act as a near field antenna. Gold films used for this purpose may benefit from a thinner film than what is typically used in SPR imaging applications ($\sim$45 nm)(Chiu et al., 2011). Efficient excitation of SPP modes in a Kretschmann geometry is more of a concern in the latter while a decreased barrier for radiation generated near the interface must also be considered in the former. The ability for the gold film to fulfill these roles is critically dependent on its thickness and surface quality.

1.3 Gold thin films

Theoretical descriptions of SPP's often involve an idealized representation of the metallic films that support them. Typically, a perfectly smooth infinite plane of arbitrary constant thickness containing a free electron gas. In reality, specific film deposition methods impose distinct deviations from uniformity. The band structure of the metal layer is also an important factor in describing optical properties of the film which extend beyond a free electron gas model.

Thin metal films stand at the boundary between familiar bulk metallic properties and an ultra thin regime where the optical and electrical properties become highly dependent on the geometry of the film, and its inhomogeneities. Many optical properties of bulk metals can be attributed to a large density of electrons which are nearly free to move throughout the interior of the metal. The responsiveness of these charges to electromagnetic fields near the surface allows efficient re-radiation of incident light, resulting in highly reflective surfaces as incident fields decay rapidly in the metal due to the lossiness of the layer. As the thickness of a bulk metal slab decreases to length scales comparable to the skin depth of the metal ($\sim$25nm for gold in near and mid IR,(Olmon et al., 2012)), the film becomes increasingly transparent as exponentially decaying fields generated at the incident face are able to reemerge as propagating waves on the opposing side. Gold films transmitting a noticeable amount of light are less than $\sim$40 nm. The penetration depth of 1000nm light is about 13 nm while 500nm light has a penetration depth of 70nm (Loebich, 1972). This notion led to early use of gold films as a cold-coating for plate glass windows, as it reflects heat from IR wavelengths while transmitting visible light.

Observations of photoluminescence from gold films under visible illumination point to optical properties that cannot be attributed to a free electron model.(Mooradian, 1969) The broad spectrum generated does not depend on excitation wavelength, suggesting a recombination of holes and electrons via interband transition between the d-valence band and sp-conduction band of gold.(Beversluis, Bouhelier, and Novotny, 2003) The X and L symmetry points in the Brillouin zone of bulk gold show a high density of states, facilitating transitions from the d band to the sp-conduction band. Energies of 1.8 eV and 2.4 eV respectively separate d holes from the Fermi surface. (Beversluis, Bouhelier, and Novotny, 2003) For near-IR sources (780nm), the surface morphology of the gold film has a strong effect on the observed spectrum, as only roughened films show a strong visible emission from two photon absorption.(Boyd, Lu, and Shen, 1986)

In the regime of negligible photon momentum, interband transition rules place constrictions on electron hole recombination that translate to inefficient emission. The efficiency of these transitions increases as photon modes of greater momenta are introduced, providing a mechanism for momentum matching additional electron-hole pairs. Modes of sufficient momentum to allow efficient two photon absorption require enhanced and spatially confined fields generated by inhomogeneities in the gold film. The range of potential sources for this film inhomogeneity naturally appeals to sensing applications, and while wide field illumination of a gold film with SPP's is not uncommon, the visible two photon fluorescence of the film itself as an indicator of the presence of surface bound analytes has not been fully utilized.

This has inspired the development of a new type of optical sensor suitable for registering the binding/dissociation of nanoscopic particles near a gold sensing surface. The method shares similarities with surface plasmon resonance microscopy but uses a completely different optical signature for reading out binding events. This new optical read-out mechanism, called confined optical field enhanced fluorescence emission (Cofefe), uses pulsed surface plasmon polariton fields at the gold/liquid interface that give rise to confined optical fields upon binding of the target particle to the gold surface. The confined near-fields are sufficient to induce two-photon absorption in the gold sensor surface near the binding site. Subsequent radiative recombination of the electron-hole pairs in the gold produces fluorescence emission, which can be captured by a camera in the far-field. Bound nanoparticles show up as bright confined spots against a dark background on the camera. The Cofefe sensor is capable of detecting gold and silicon nanoparticles, as well as polymer nanospheres and lipid droplets in a label-free manner.

Chapter 2

Wide field excitation of SPP's on gold films

2.1 Introduction

The complex dielectric function of gold provides an analytical quantity for describing the electrical and optical properties of thin films ($\varepsilon \sim -25.6 + 1.6i$ at 817 nm) . In the case of propagating modes along the x direction at a metal/dielectric interface, the dispersion relation may be expressed in terms of the wavelength dependent dielectric constants of each material. Quantities such as the SPP coupling angle in a Kretschmann configuration, which matches the in-plane component of the incident field momentum to the in-plane SPP momentum for a given frequency, may also be expressed in terms of the dielectric constants of the corresponding three layer system.

$$k_x = \frac{\omega}{c}\sqrt{\frac{\varepsilon_1\varepsilon_2}{\varepsilon_1+\varepsilon_2}} \tag{2.1}$$

$$\theta_{SPP} = \sin^{-1}\left(\frac{1}{n_3}\sqrt{\frac{\varepsilon_1\varepsilon_2}{\varepsilon_1+\varepsilon_2}}\right) \tag{2.2}$$

In terms of the real and imaginary components of the in-plane momentum, k_x, we obtain the following expression.

$$k_x = k_x' + ik_x'' = \left[\frac{\omega}{c}\left(\frac{\varepsilon_1\varepsilon_2'}{\varepsilon_1+\varepsilon_2'}\right)^{\frac{1}{2}}\right] + i\left[\frac{\omega}{c}\left(\frac{\varepsilon_1\varepsilon_2'}{\varepsilon_1+\varepsilon_2'}\right)^{\frac{3}{2}}\frac{\varepsilon_2''}{2\left(\varepsilon_2'\right)^2}\right] \tag{2.3}$$

Similarly, the momentum of the SPP field in the z direction away from the interface may be expressed as the following.

$$k_z = \frac{\omega}{c}\sqrt{\frac{\varepsilon_2^2}{\varepsilon_1+\varepsilon_2}} \tag{2.4}$$

As the SPP propagates along the film, energy is lost due to ohmic losses in the film. The characteristic propagation length, L, of an SPP is associated with the imaginary component of the dispersion relation ($\sim 50\mu$m for 817 nm with an air interface).

$$L = \frac{1}{2k_x''} \tag{2.5}$$

The decay of the field away from the interface into the dielectric material determines the effective probing volume in SPP based microscopes. The penetration depth of

the SPP into the metallic surface is generally smaller due to the lossiness of the film and effects the degree of leakage radiation that is detected in a Kretschmann configuration. In the equation below, the index i refers to the metallic side ($i = 1$) of the interface or the dielectric side ($i = 2$).

$$z_i = \frac{\lambda}{2\pi} \left(\frac{|\varepsilon_2'| + \varepsilon_1}{\varepsilon_i^2} \right)^{\frac{1}{2}} \tag{2.6}$$

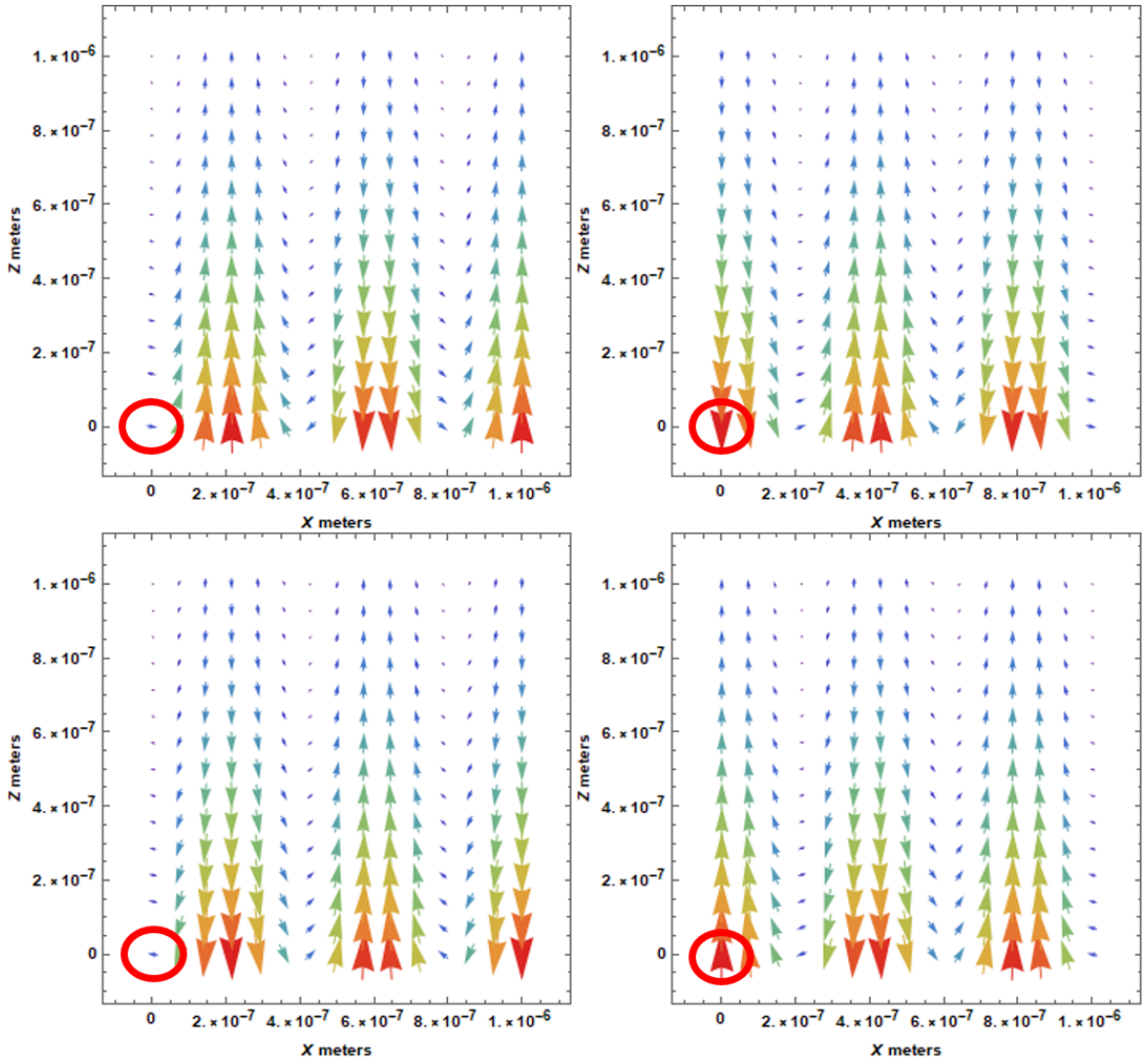

FIGURE 2.1: SPP field at time intervals of T/4 displaying an elliptically polarized field with greatest magnitude in the direction away from the interface

The full time dependent expression for the propagating SPP field, neglecting losses in the film, may be expressed in the form in eq. 2.5. As seen in Fig. 2.1, the field propagates in the positive x-direction and decays in magnitude away from the interface. Four equally spaced time intervals over one period T are displayed. Focusing

on a single spatial coordinate demonstrates the elliptical nature of the field. The ellipticity of the field depends on both wavelength and the dielectric constants of the materials at the interface. In the case of gold excited by 817 nm light, the field can be seen to be nearly polarized perpendicular to the interface.

$$E[x,z,t] = \left(1, 0, -\frac{k_x}{k_z}\right) e^{i(k_x x - \omega t + k_z z)} \tag{2.7}$$

Numerous experimental measurements of dielectric constants across thickness, and incident wavelength reveal a complicated material response dependent on the band structure of gold as well as the preparation dependent inhomogeneities across films. Ellipsometry measurements by Olmon et al on thermally evaporated 200nm thick gold films safely fall within the bulk regime and point to intraband transitions at lower energies and an onset of interband contributions in the visible region(Olmon et al., 2012). Measurements on thin films ∼25-50nm show a characteristic thickness above which dielectric constants of gold do not change drastically from their bulk values(Johnson and Christy, 1972). In the ultra-thin regime, measurements of dielectric properties become inconsistent and begin to deviate from their bulk values.

This is in part due to the difficulty in producing homogeneous and uniform thin films. Vapor deposition is a common method for producing metallic films for microscopy applications. The simplest way to incorporate SPP's into a microscope is to add a negligible amount of evaporated gold to a standard BK-7 glass coverslip. Typically an adhesion layer (∼1–2nm Cr) is required to bind the gold layer to the substrate. Substrate material, preparatory cleaning procedures, temperature during evaporation, film thickness, all can effect the resulting surface morphology.

Ultra-thin films often consist of disconnected islands as opposed to a two dimensional film. Unsurprisingly, these films are highly transmissive and have very low electrical conductivity. Continuous gold films down to thicknesses of ∼5nm have been achieved on fused silica activated with mercapto-silane to promote Au adhesion using high deposition rates,∼10 Angstroms/sec. The optical constants of these films still show deviations from bulk values that are difficult to assign to morphological properties of the film however(Kossoy et al., 2014). Silicon substrates offer a more uniform substrate than BK7 coverslips but the lack of transparency limits their use in many microscope configurations. Mica also provides a flatter surface than glass and is ultra clean after removal of a thin layer of mica before deposition. The benefit of a freshly cleaved surface, however, complicates quantification and repeatability due to the uncertainty in substrate thickness. Template stripped films have been shown to produce high quality gold thin films but involves a mechanically robust transparent substrate with an adhesive layer to peel a gold film from an atomically flat opaque surface. The mechanical strain involved in peeling the substrate requires a thick glass layer that can be outside of the working distance of high NA objectives, and the necessary addition of an epoxy layer complicates interpretation of the optical properties of the entire three layer structure. Practical applications of SPP's not only require a careful consideration of the particular surface morphology for a given production method but also how SPP's interact with characteristic surface features.

2.2 Methods

Two laser sources are used in the experiments described in this chapter. The first consists of a 76 MHz Nd-Vanadate amplified oscillator (PicoTrain, High-Q), which produces 7 ps pulses at a center wavelength of 1064 nm. A portion of the output is frequency doubled and used to synchronously pump an optical parametric oscillator (OPO, Levante Emerald, APE-Berlin). The latter delivers tunable radiation in the 750–950 nm range. The second light source is a Titanium:sapphire laser (Mira900, Coherent), which produces a 76 MHz pulse train of $\sim$150 fs pulses. For the experiments discussed here, the picosecond source is tuned to 817 nm, and the femtosecond wavelength is set to 810 nm.

The near-IR beams are conditioned with a spatial filter and expanded to a $\sim$7 mm beam diameter, exhibiting a Gaussian transverse profile that is linearly polarized. A 200 mm achromatic lens (Edmund Optics) focuses the beam on the back focal plane (BFP) of a 60x 1.49 NA oil immersion objective, (APON60XOTIRF, Olympus) providing wide-field illumination

The focusing lens is attached to a movable mirror that translates the lateral position of the focused spot on the BFP, resulting in an angular adjustment of the collimated beam incident on the coverslip. In this configuration, the diameter d of the illuminated field of view (FOV) can be estimated from the following ratio:

$$d_{FOV} = d_{beam} \frac{FL_{\text{objective lens}}}{FL_{\text{focusing lens}}} \tag{2.8}$$

where FL denotes focal length. In the picosecond experiments described here, the FOV is set as 105x105 μm^2.

Sample substrates consist of borosilicate glass coverslips (BK-7, VWR) coated with gold. Gold thin films are evaporated to a thickness of 30 nm on borosilicate glass coverslips (BK-7, VWR), which are pretreated with a 2 nm Cr adhesion layer. For patterned Au films, lithographic masks are used for depositing S1808 photoresist (Shipley) onto the surface, followed by chemical etching, creating patterns consisting of 20 μm wide Au stripes, with a spacing of 20 μm between the stripes.

2.3 Results

2.3.1 Wide-field excitation of SPP modes

To generate the surface-bound SPP excitation field, the freely propagating near-IR beam has to be coupled to the surface plasmon mode. We have chosen an objective-based Kretschmann configuration, in which the beam is incident on the gold/air interface at the SPP coupling angle of $\theta = 42.3^o$.

The alignment of the beams is facilitated by monitoring the backreflection of the excitation beams onto the CCD camera. Figure shows the backreflection of the beam at 817 nm incident on a striped gold film. In Fig 2.2 , the coupling angle is below the Kretschmann angle, resulting in a strong reflection at the gold stripe (bright) and a weak reflection from the bare glass (dark). When the incident angle is tuned to $\theta_{pump} = 42.3^o$, phasematching with the SPP mode occurs and energy is transferred

from the freely propagating mode to the surface-bound mode. The latter can be inferred from Fig 2.2 , which shows greatly reduced reflection at the gold stripe, whereas the signal from the exposed glass is elevated due to total internal reflection. As in previous surface plasmon resonance microscopy studies (Halpern et al., 2014), efficient SPP coupling is achieved over the entire FOV.

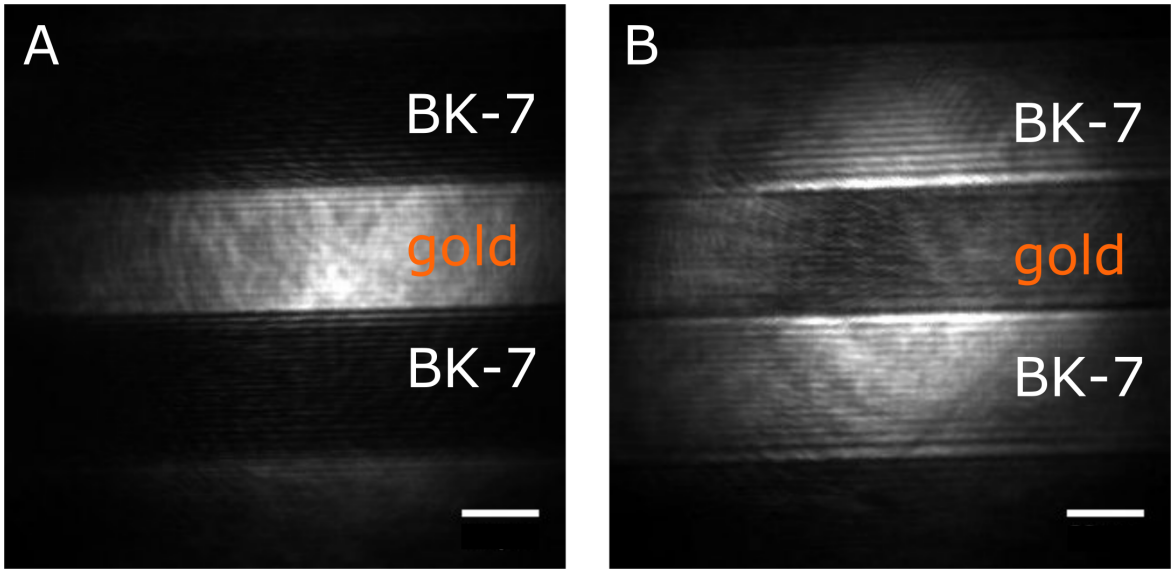

FIGURE 2.2: Coupling of light to SPP at the gold film-air interface. Reflection image of the beam at 41^o, before light couples (A) and at 42.3^o when energy transfer to the SPP mode occurs (B). Scale bars are 20 μm.

The field enhancement generated relative to the incident field is far less than what is observed in SERS and TERS where electromagnetic fields are confined to a nanoscopic volume which may provide enhancement factors on the order of 10^{10}(Le Ru et al., 2007). Field confinement in the axial dimension alone is expected to produce a more modest enhancement at any given point on the film. In the FDTD simulations depicted in Fig. 2.3 , the enhancement of a near-IR beam at an metal/water interface is

$\sim$ 5-7. It is important to note that this does not predict the full enhancement achievable with flat metallic films as SPR experiments typically use thicker films than the 30 nm thickness used in these experiments. Numerical arguments show that for a gold film excited in a Kretschmann configuration, optimal enhancement is achieved with films that are near 50-70 nm thick.(Fontana, 2006)

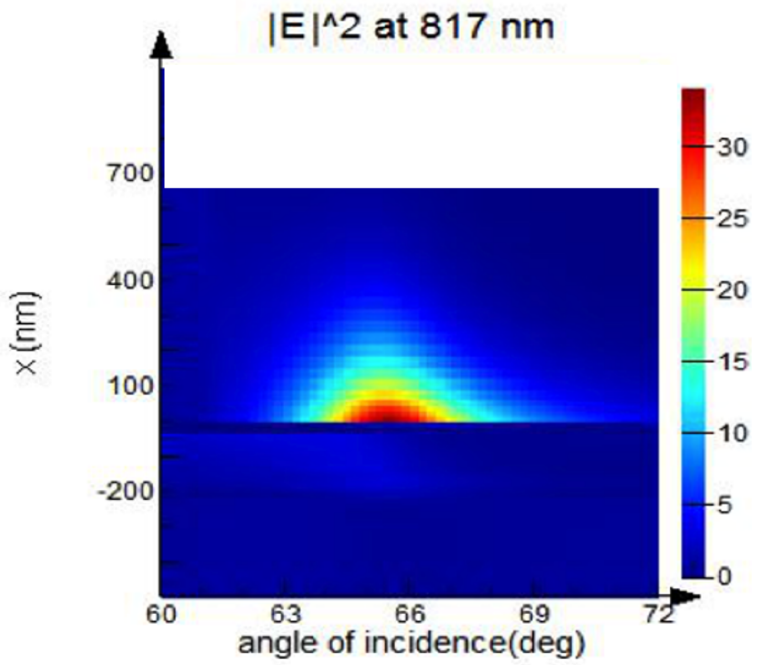

FIGURE 2.3: Field intensity above the gold film as a function of indidence angle for a 30nm Au film

While a thicker film may couple more efficiently to SPP modes, thinner films may experience greater leakage radiation which is more desirable for certain applications such as SPCE. Field enhancement in a Kretschmann configuration with a 50nm gold film has been theoretically estimated as $\sim 10^2$(Meyer et al., 2012). It is also worth noting that reports of SERS enhancement on flat films are typically $\sim 10^3$-10^4

(Meyer et al., 2012). Reciprocity arguments suggest that the same mechanism that enhances the incident field will also enhance the detected raman signal. Evidence of this effect may also be present in the experiments described below.

2.3.2 Gold film fluorescence

Interestingly, the addition of non-fluorescent biological materials to the gold surface surface results in an unexpected emission. The figure below demonstrates that a clear signal can be obtained from lipid droplets. The image is free from diffraction patterns that are often associated with SPRI where changes in refractive index at the surface produce interference effects with the reflected incident beam. In fact the signal persists even with the presence of a band pass filter centered at 660 nm which blocks the incident wavelength, excluding the SPRI mechanism as the source of the signal. The broadband nature of the signal and the absence of interference artifacts suggest a fluorescence process, and yet it is still observed for samples that are incapable of autofluroescence. Further studies suggested that the signal originates from the film itself in the vicinity of the sample.(Fast et al., 2016)

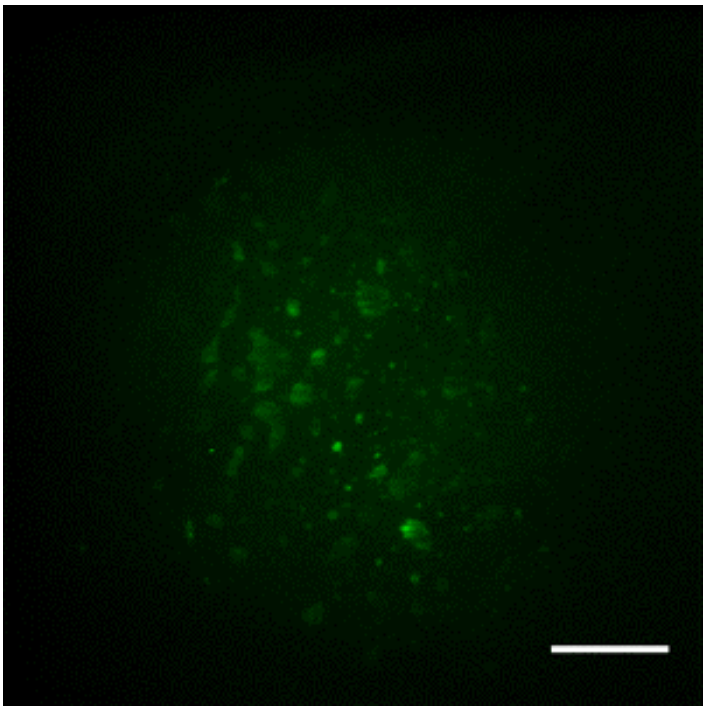

FIGURE 2.4: Lipid droplets on the surface of a gold film illuminated by 817nm picosecond light incident at the SPP resonance angle. A bandpass filter 660/40, is used to isolate the fluorescence signal from the incident light field

Fig. 2.5 shows another example of lipid droplets adhered to the surface, illuminated with an 800nm fs source, and the corresponding back focal plane image. By placing a Bertrand lens in the detection path, the distribution of emitted photon momentum can be projected onto the CCD. The bright ring apparent in the BFP image is characteristic of leakage radiation from SPP fields, corresponding to a specific k-vector(Drezet et al., 2008; Bharadwaj, Bouhelier, and Novotny, 2011). The rings appearance through the bandpass filter suggests that the detected emission couples to SPP modes before outcoupling to the far field, as opposed to leakage of the incident SPP.

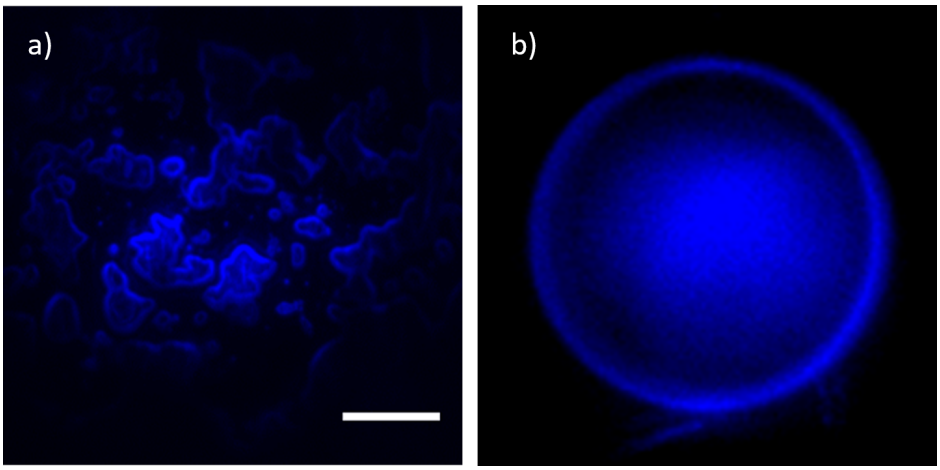

FIGURE 2.5: a) Cholestorol Oleate adhered to the surface. b) Back focal plane image corresponding to a).

In SPP based microscopes this signal may be considered an undesirable background effect.(Fast et al., 2016) The ability to localize particles at the surface with high signal to noise raises the possibility of label free sensing applications. In able to translate this effect to practical sensing methods, a better understanding of the sensing surface itself is required. Another prominent observation from gold films is the strong outcoupling of light from seemingly random locations on a bare sensor surface. SEM images reveal that the source of this emission is from inhomogenites in the film.

2.3.3 Film defects and hotspots

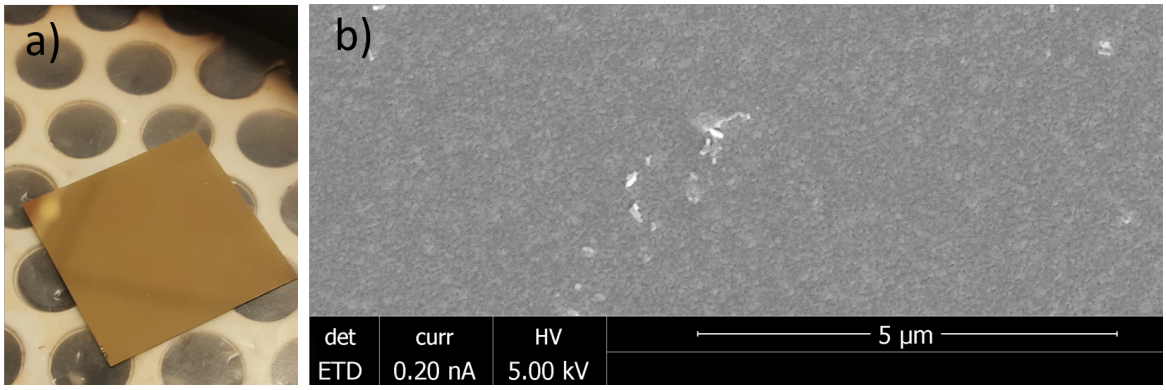

FIGURE 2.6: a)Typical gold coated coverslip produced by vapor deposition. b) SEM image of a gold coverslip surface with high density of defects

Exciting SPP fields over a wide field of view presents challenges in terms of film quality. Instead of film smoothness on the grain level of the film, the concern is uniformity of the film over large areas (100μm x 100μm). Gold protrusions and pinholes in thin films have been well documented across multiple film production techniques, and many methods of minimizing their presence have been suggested. Defects in the film result in "hotspots" that strongly out-couple light from the SPP fields. Even high quality films can not completely exclude these inhomogeneities, highlighting the importance of quantifying their emission properties. Fig. 2.6 shows an example of a typical surface feature. Under thermal vapor deposition, the surface quality varies greatly with preparation method and may not be uniform within the same batch or even within different areas of a single coverslip. Isolated gold defects react strongly with SPP fields on the surface, and can dominate the entire field of view for surfaces with a high density of defects. The ability to consistently produce

films with minimal defects over large areas will be key to distinguishing effects observed in surface bound samples from emission associated with inherent surface features.

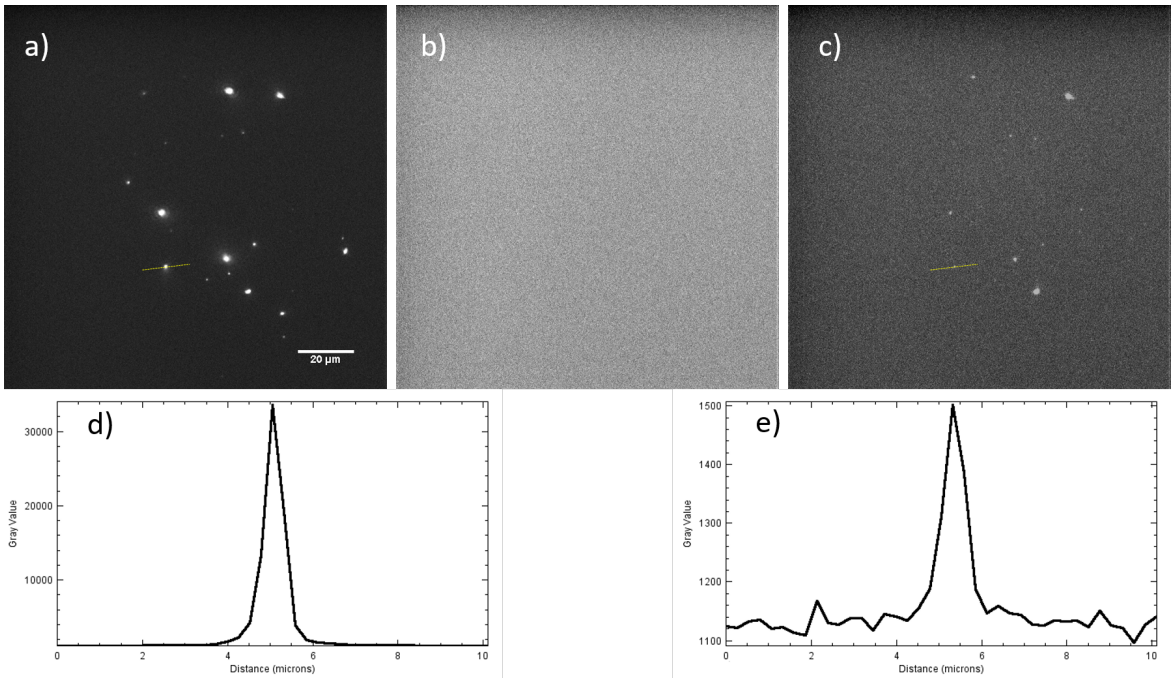

FIGURE 2.7: a) Outcoupling of light from surface defects under SPP illumination from 150 fs, 50 mW pulses b) Same region as in a), illuminated with 50 mW of CW light. c) Outcoupling produced by 360 mW of CW light

The low powers used in typical SPRI microscopes along with difference imaging schemes and a small detection window around the excitation wavelength, limits the broadband response of hotspots. For comparison, a bare gold film was illuminated with both a CW and 150 fs pulsed laser to demonstrate the effects of high peak fields on emission from surface defects. A bandpass filter (625/90) is included in the CCD detection path to filter out incident light from the image. With a pulsed

source at 50 mW surface defects appear as very bright spots, registering ∼30,000 counts on a CCD camera over a 1 second exposure, accumulated over ten frames. In CW mode, 50 mW produces no detectable signal. Increasing the CW power to 360 mW results in clear emission from the same surface defects but only registers ∼1500 counts, nearly 20 times less than the pulsed beam at much lower average power. Clearly, excitation of SPP fields with pulsed sources requires a high degree of surface uniformity to allow for easy distinction between emission from film hotspots and signals originating from the position of sample material at the surface.

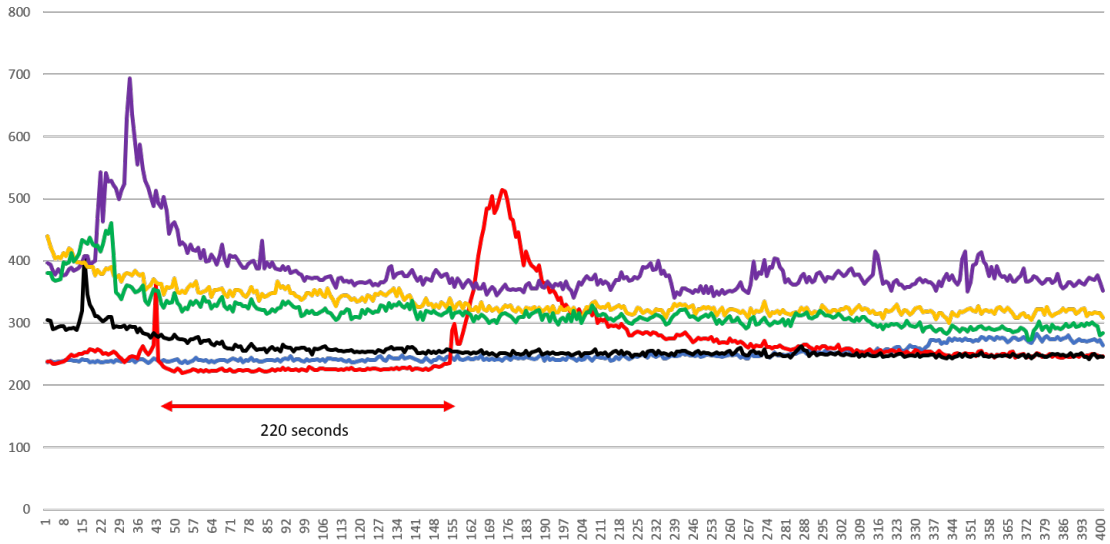

FIGURE 2.8: Intensity of hotspots on the gold film surface as a function of time.

Emission from defects also show irregular behavior in time. Occasional blinking effects are observed but the most common observation is an intense emission that appears directly after illumination which then decays on the timescale of seconds. A

much smaller set of hotspots do not reach peak intensity until minutes after illumination, potentially complicating interpretations of dynamic sample related events at the surface. The equilibrium intensity for hotspots shows a great deal of variability with higher equilibrium values corresponding to higher initial peak intensity, potentially reflecting the relative size of the defects. Similar effects are observed when gold nanoparticles are adhered to the gold surface, which provide a more uniform source for studying decaying and intermittent emission properties.

2.3.4 Gold particles in air

Both gold nanospheres and surface protrusions contain a large number of free electrons and have the potential to support localized surface plasmons, generating intense fields in highly confined spaces. Gold nanospheres and their plasmonic behavior have been well documented and can potentially provide some insight into the observed time profile from surface defects.

Temperature effects are an important factor in the spectra of metallic nanoparticles. Heating effects, caused by intense localized fields, have the potential to change observed emission properties under continuous illumination. A temperature increase in solution surrounding a gold nanoparticle will alter the refractive properties of the solution, resulting in a decrease in the intensity of the plasmon resonance (Link and El-Sayed, 1999). Gold particles embedded in a glass matrix have been heated over a wide temperature range and demonstrate a decrease in intensity of the plasmon absorption spectra with increasing temperature as well as a redshifting of the peak (Link and El-Sayed, 1999). This behavior can be rationalized through temperature

dependent Mie scattering (Kreibig, 1977). Similar observations have also been attributed to a decreased electron concentration at higher temperature, resulting in a modified spectrum (Doremus, 1964). Studies have shown that significant alteration of the spectrum requires a change of several hundred degrees (Link and El-Sayed, 1999). To limit the effects of solution temperature in the observed decays, hotspots and 100 nm gold spheres excited in air were recorded in time. In both cases, a decay from their initial intensity was observed.

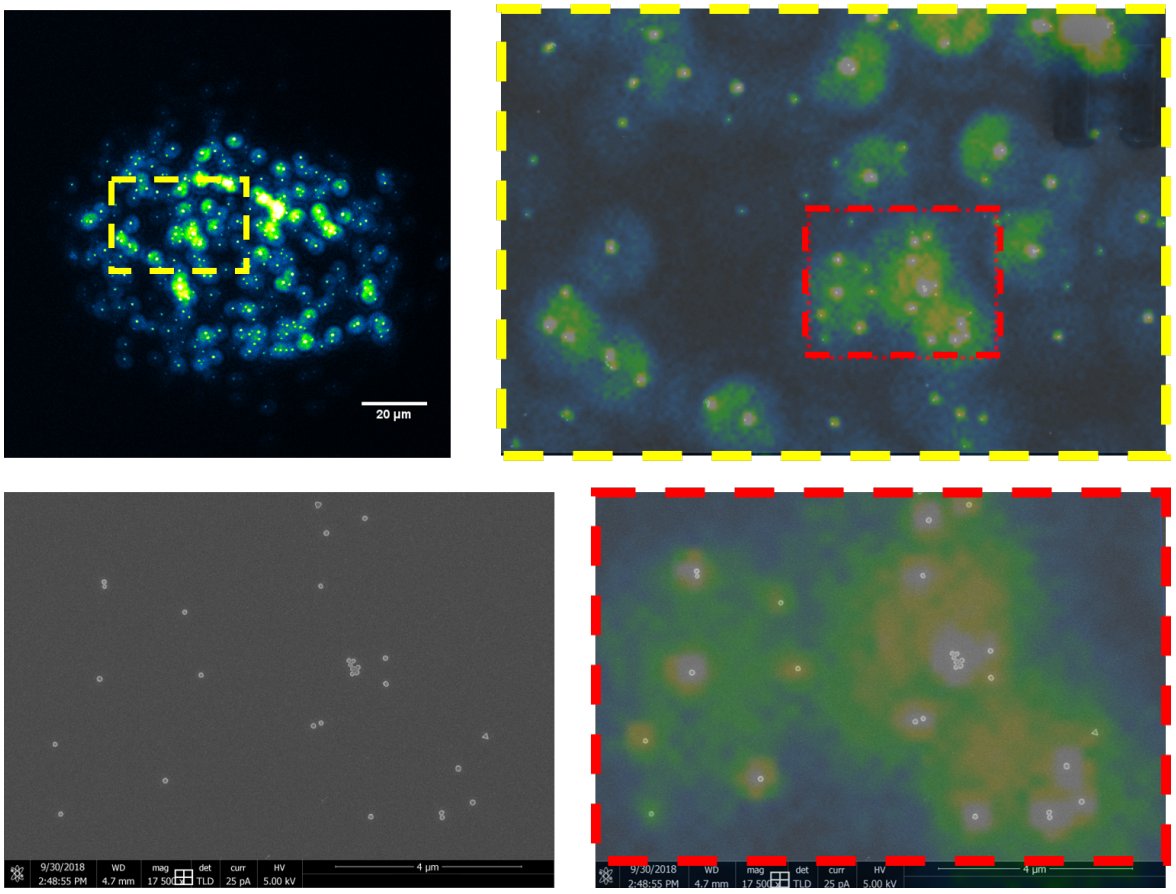

FIGURE 2.9: a) Signal image from 100nm Au in air adhered to the film surface. b)d) Overlay of signal with SEM image. c) SEM image of region of interest.

Another consideration is the heat generated within the particle and the supporting film which may be high enough to induce melting, altering the spheres shape and thus changing its plasmonic spectrum(Kuhlicke et al., 2013). Melting a spherical particle would intuitively form a flatter shape on the gold film where a largely p-polarized SPP field on the film surface would be applied along a shorter axis of the particle, resulting in reduced scattering intensity. To investigate this possibility, SEM images of 100 nm Au particles adhered to the gold surface were taken before and after illumination at various powers. Even after high levels of SPP irradiation, the gold particles do not show any obvious signs of morphological changes due to heating. Temperature modifications to the particle can not be excluded entirely due to the limited resolution of the SEM images taken. Unresolvable features that are too small or are on the underside of the sphere are likely to experience the largest localized field enhancements and thus are more likely to be modified by heating effects. In general, temperature induced shifts in the emission spectrum may exaggerate reduction in intensity due to signal collection through a fixed band pass filter.

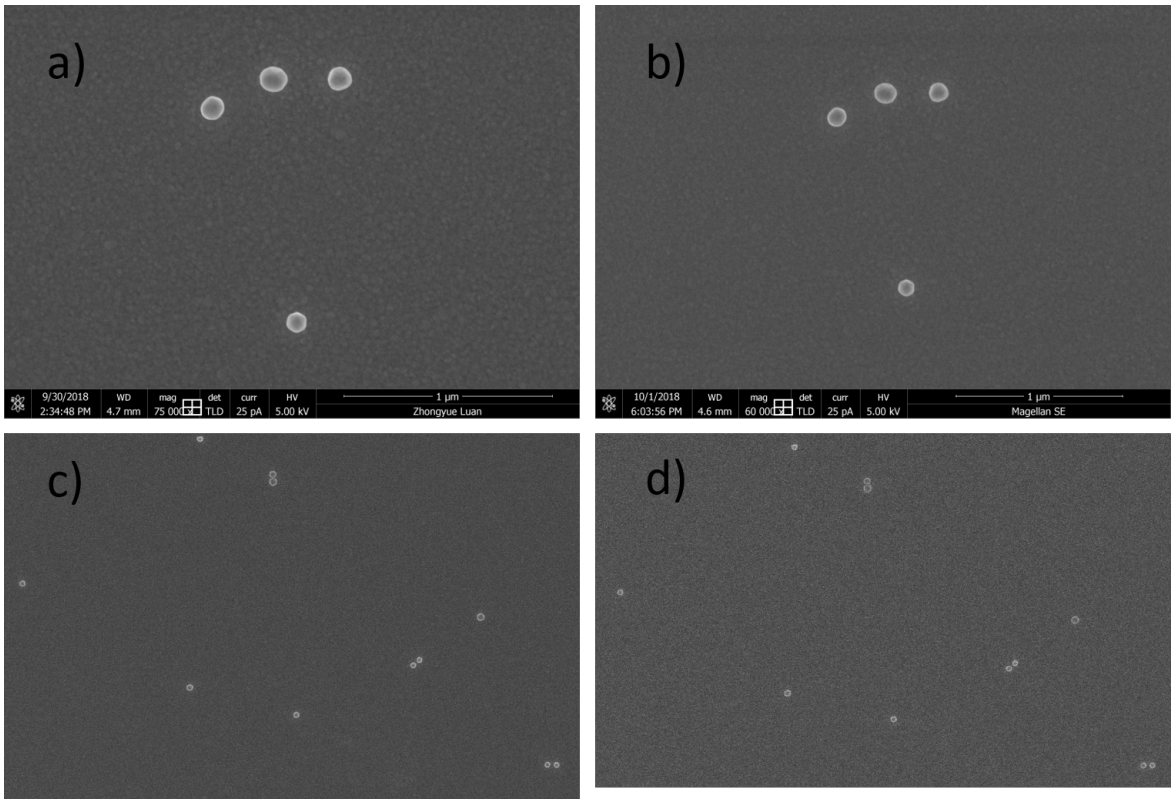

FIGURE 2.10: a)b) Before and after images of 100nm Au particles illuminated with 10mW for 100 seconds c)d) Before and after images of 100nm Au particles illuminated with 160mW for 100 seconds

Photo-blinking of gold nanostructures under CW illumination have been previously reported in the literature. Photo-bleaching effects have been documented as well(Li et al., 2017; Yuan et al., 2016), though not in all reports involving blinking effects. Sinlgle photon luminescence experiments on nano-sea-urchins (NSU) using CW sources have shown that the enhanced fields generated by surface plasmon resonances confined to the sharp spine features of the nanostructure result in blinking effects(Su et al., 2010). Similar observations have been made on gold nanospheres ($\sim$ 15-20 nm) and individual nanoclusters ($\sim$ 2 nm)(Li et al., 2017; Yuan et al., 2016).

The proposed emission mechanism begins with a recombination of d-valence band holes with sp-conduction electrons, which are excited by a single photon. In some instances, the excited hole may recombine with another electron before the excited electron is scattered near the Fermi surface. The energy released in this Auger process is heat energy as opposed to a photon, leading to a "dark" state observed in blinking. Occasional blinking effects are observed under SPP illumination but are relatively rare compared to the exponential decay behavior.

In this experiment, a reduction of intensity with no clear off state is observed. Thermal relaxation times associated with gold nanoparticles are ultrafast and can not directly explain the long decay times observed here. Decays over long periods of time have been reported in emission from ensembles of gold nano-clusters under ambient environmental conditions(Yuan et al., 2016). Curiously, the decay was not observed while nano-clusters were immersed in solution. Individual nanoclusters on the other hand do not decay but blink and eventually bleach. TEM images have demonstrated that Au nano-spheres contain crystaline domains that may act as separate emitters, contributing to the same diffraction limited spot on the camera (Li et al., 2017). This further relates emission from a nanocluster ensemble to 100nm spheres, although the set of domains within the particle is expected to form a rather small ensemble.

In the case of SPP excited Au nanoparticles, environmental heating effects are introduced either through direct heating of the solution by excitation fields, or through heat produced by the film or the particles themselves. The plasmonic spectrum is expected to be modified. SEM imaging after intense irradiation demonstrates

that temperature changes do not create drastic changes to the shape of the material. Blinking events suggest that nanoparticles under intense illumination may release energy through optically non-radiative modes, and slow decay times may reflect an ensemble measurement of emitters within the same nanoparticle. All these factors must be considered in the observed emission. Further measurements of power dependence and particle size on emission time profiles may be helpful in characterizing the underlying physics involved.

2.4 Conclusion

SPP fields can be efficiently driven over a wide area of a thin gold film using high N.A. objectives and near-IR sources. Coupling to the SPP resonance angle becomes more challenging as the index of refraction of the dielectric layer increases. As the coupling angle increases, the incident beam must be displaced farther from the optical axis of the objective. For samples in solution this imposes precise alignment requirements but remains within reach of high NA objectives. The resulting excitation field provides a novel method for probing the region just above the film with intensities that are expected to produce nonlinear light-matter interactions that may be detectable when light fields with sufficient peak intensities are used. The film itself can become a source of fluorescence emission in regions where SPP fields become locally enhanced and may be induced by a target particle adhered to the film or inherent surface features of the film. Both contributions must be accounted for in further applications of this setup.

Chapter 3

COFEFE

3.1 Introduction

Surface plasmon resonance (SPR) sensing is a technology used for measuring binding and dissociation kinetics of biomolecules at a gold sensor surface.(Zhang and Uttamchandani, 1988; Homola, Yee, and Gauglitz, 1999; Boozer et al., 2006; Homola, 2008; Phillips and Cheng, 2007) Such biomolecular interactions include interactions among proteins, peptides, nucleotides, sugars and other molecules. In pharmaceutical, clinical and biotechnological research, for instance, knowledge of biomolecular interactions is key in determining efficacy of a drug, understanding immunological responses or discovering new therapeutic targets, to name just a few.

Whereas the SPR technique is very sensitive, its common implementation is unable to detect individual binding and dissociation events. Kinetic SPR data is typically the result of ensemble averaging over many events, integrated over both space and

time. Consequently, rapid on/off events at particular sites on the sensor surface are not registered, as they are averaged out by the slower dynamics of the ensemble. Other unexpected binding patterns at particular sites also go unnoticed. Such outlier behavior can be important, as these events may signify functional aspects of the molecular interaction, related to particular conformations, density related binding kinetics or other effects of direct relevance. The ability to see all binding/dissociation events in parallel would significantly enhance the analytical capabilities of the SPR sensor.

Individual binding/dissociation events can be studied with a microscopic imaging version of SPR, namely surface plasmon resonance microscopy (SPRM).(Jordan et al., 1997; Brockman, Nelson, and Corn, 2000; Kano and Knoll, 2000; Huang, Yu, and Zare, 2007; Weichert et al., 2010) The latter technique makes it possible to visualize individual events in parallel with a camera, thus enabling multiplex detection of particles interacting at the sensor surface. SPRM has been successfully employed to probe individual cells(Wang et al., 2012), bacteria and viruses(Syal et al., 2015; Wang et al., 2010), DNA(Yu et al., 2014; Halpern et al., 2014), and protein structures.(Maley et al., 2017) The ultimate sensitivity of SPRM is limited by various factors.(Raether, 1977; Kooyman et al., 1988; Yu et al., 2017) One limitation is related to the fact that SPR methods are not background-free, as small changes in the light intensity need to be discriminated against a bright background. Another limiting factor is the non-ideal pointspread function of SPRM, which is characterized by long diffractive tails that affect the spatial resolution of the technique. To increase the spatial resolution, special algorithms have been developed that improve the performance of the SPRM device, achieving an effective resolution on the sub-micrometer scale.(Yu et

al., 2017) Nonetheless, the restored pointspread function is non-symmetric and may exhibit residual flaring.

The SPRM technology would benefit from an optical signaling mechanism that is associated with a well-behaved pointspread function and that produces a positive signal relative to a low background. In this work, we present an optical signature at the gold sensor surface that addresses the aforementioned issues. The signal, which we attribute to two-photon excited fluorescence in the gold film, is triggered by binding of particles to the surface. The pointspread function, which appears against a dark background, is incoherent and thus devoid of interferences among detected spots. The resulting technique is related to two-photon surface plasmon-coupled emission (SPCE) microscopy(Gryczynski et al., 2005; He et al., 2009), but without the need to incorporate fluorophores and thus allowing label-free probing of targets. We discuss the optical layout of this new approach and present its capabilities for detecting individual particles in the vicinity of the sensor surface.

3.2 Materials and Methods

A schematic of the sensor device is shown in Fig. 3.1. The light source is a Titanium:sapphire laser (Mira900, Coherent), which produces a 76 MHz pulse train of $\sim$150 fs pulses. In the experiments the center wavelength is set to 810 nm. The linearly polarized source is conditioned with a spatial filter to generate a clean Gaussian transverse profile of 10 mm diameter. The collimated beam is then focused by a f = 250 mm lens onto the back focal plane of a high numerical aperture objective

(NA 1.49 oil, Olympus). The resulting collimated beam emerging from the objective corresponds to a circular illumination spot with a diameter of ~ 120 μm on the sensor surface. The sensor surface consists of a borosilicate coverslip coated with a 30 nm thick gold film. By translating the beam in the back focal plane, the incidence angle of the collimated beam at the surface can be tuned to the Kretschmann angle for excitation of a surface plasmon polariton (SPP) mode at the gold/water interface ($\sim 65^o$). The resulting two-photon luminescence from the gold film is collected in the epi-direction by the objective and separated from the incident beam by a 700 nm short wave pass dichroic mirror. The signal is subsequently filtered by a 625 nm$\pm$45 nm band pass filter and 750 nm short wave pass filter. In some of the experiments, a 1.6$\times$ telescope is incorporated in the detection path for increased magnification, resulting in an image distance of 169.5 nm per pixel with a ~ 60 μm diameter field of view (FOV). Average illumination powers, determined before the objective lens, are between 12 mW and 150 mW, depending on the FOV and the sample. For each of the experiments that follow, the illumination dose is specified in $\mu W/\mu m^2$, which is independent of the FOV. Note that the actual dose at the sample is lower because of losses in the objective lens and specimen. The signal is recorded on an EM-CCD camera (iXon3, Andor) as stacks of images (512 $\times$ 512 pixels) with a frame rate of 1 fps. Higher acquisition rates may be obtained with a reduced region of interest (ROI). For instance, for a ROI of 256 $\times$ 256 pixels, the signal can be recorded at 68 fps.

Sensor surfaces consist of borosilicate glass coverslips (BK-7, VWR) coated with gold. Gold thin films are evaporated to a thickness of 30 nm on the coverslips, which are pretreated with a 2 nm Cr adhesion layer. Analytes used in this experiment

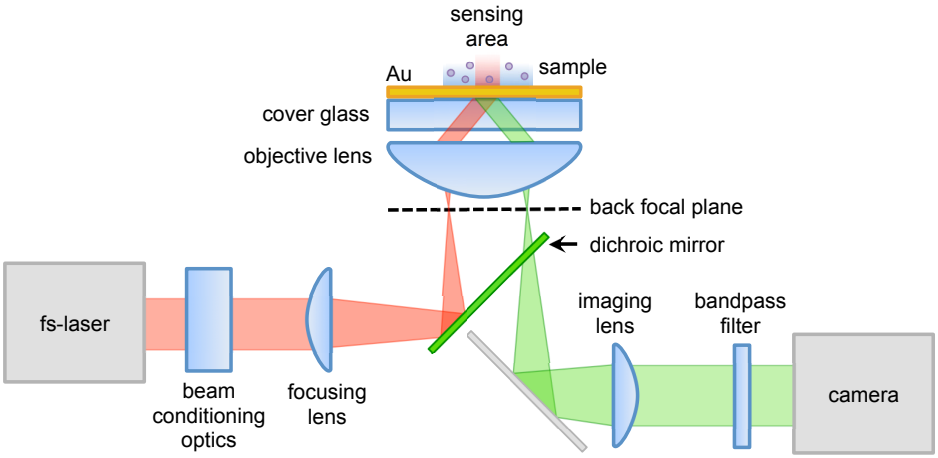

FIGURE 3.1: Schematic of the sensor device. A fs-laser beam is focused on the back focal plane of a high NA objective lens, launching an SPP field at the sensor surface. Particle binding gives rise to local two-photon excited fluorescence in the gold film, which is captured by an imaging camera.

included gold spheres (10 nm, 20 nm, 30 nm), cholesteryl oleate droplets (Sigma Aldrich), polystyrene spheres (350 nm from Thermo Fisher), and silicon nanoparticles (30 nm, Melorium Technologies). All particle suspensions are diluted in milli-Q filtered water and sonicated before use. Lipid droplets are formed by preparing an emulsion of cholesteryl oleate with phosphatidylcholine in phosphate-buffered saline (PBS). Using $\sim$ 50 μL of a stock solution, the emulsion is subsequently drop cast on the Au-covered microscope coverslips, resulting in air-dried droplets and micrometer-sized polymorphous crystals of cholesteryl oleate on the surface. The structures were re-immersed in milli-Q filtered water before inspection with the imaging sensor. Si particles, gold spheres, and PS spheres were all diluted with deionized water and drop cast onto gold-coated coverslips.

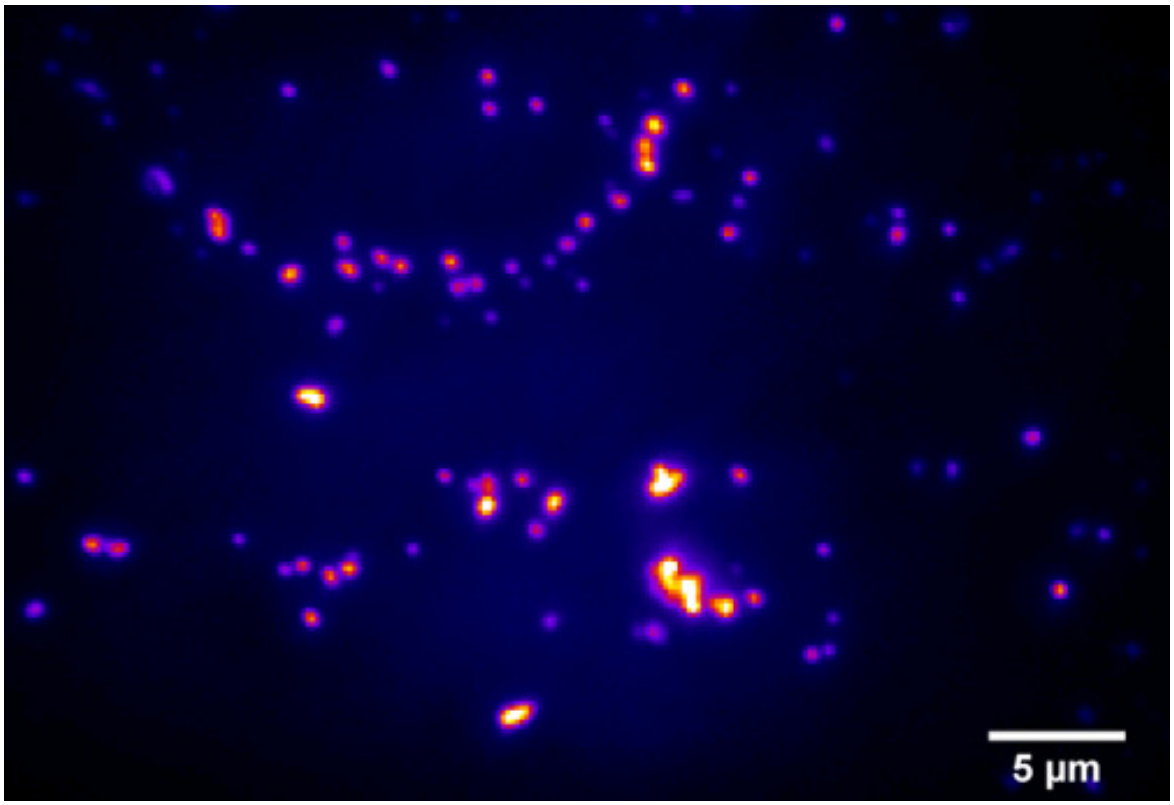

FIGURE 3.2: Gold nanospheres (20nm) adhered to the sensor surface in an aqueous medium. Average power of the illuminating beam before the objective lens is 15 mW.

3.3 Results

3.3.1 Detection of gold nanoparticles

We first examine the signal from a bare gold film on glass, using milli-Q filtered water as the sample. For smooth, freshly prepared films, the background signal is near or at the dark count rate of the camera, approximately 100 counts/s. This latter observation indicates that the signal from the bare gold film is very small. However, for older sensor surfaces and at higher illumination doses (up to 28 $\mu W/\mu m^2$), the

signal from the bare sensor can reach 370 counts/s.

When gold nanoparticles are deposited on the sensor surface, bright spots are detected that are well above the background. A representative result is depicted in Fig. 3.2 , which shows the detected image on the camera after 20 nm gold particles are physisorbed to the sensor surface from solution. The image is only visible when the incident beam is coupled to the gold film at the Kretschmann angle. Small detuning away from the coupling angle results in the disappearance of the signal. Signal is only observed when particles are adhered to the surface, particles suspended in the bulk remain invisible. We observe similar results for gold nanospheres of diameters of 10 and 30 nm.

In Fig. 3.2, the signal is accumulated over 100 raw frames taken at 68 fps by using a 256×256 ROI of the camera chip (60 μm diameter on the sensor surface) with a 15 mW beam incident on back aperture of the objective lens, corresponding to 5.3 $\mu W/\mu m^2$ average power or less than 78 $nJ/\mu m^2$ average energy for each raw frame. Signals clearly distinguishable from the background are still observed when the illumination power is lowered. For instance, at 68 fps, average illumination powers of 5–10 mW (1.8–3.5 $\mu W/\mu m^2$) produce images with detected spots well above the background counts in each frame. When the electron-multiplying (EM) gain is used, with a gain between 25 and 300, illumination powers can be lowered to 1–2 mW (0.36–0.71 $\mu W/\mu m^2$) at the same acquisition speed.

Gold nanoparticles, which are commonly used in SPRM experiments as contrast enhancers, support localized surface plasmons. The enhanced fields associated with the surface plasmon mode can give rise to two-photon excitation of electron-hole

pairs in the gold particle, followed by fluorescence emission upon electron-hole recombination.(Mooradian, 1969; Boyd, Lu, and Shen, 1986; Beversluis, Bouhelier, and Novotny, 2003) Whenever a gold nanoparticle lands on the sensor surface, the local fields are even more enhanced by the nanocavity formed between the particle and the gold layer. It is, therefore, perhaps not surprising that strong fluorescent signals from the location of the particles are observed. The results shown in Fig. 3.2 demonstrate that the nanocavities between the analyte (particle) and the gold film are efficiently excited by the SPP modes on the sensor surface, and that the resulting incoherent emission is conveniently detected by the far-field camera. Next, we examine whether similar results can be obtained for particles that do not support localized surface plasmon modes themselves.

3.3.2 Detection of semi-conducting nanoparticles

We use 30 nm silicon nanoparticles as non-metallic particles for examining the sensitivity of the sensor to nanoparticles that do not support localized surface plasmon modes. As a consequence, we expect signals that are weaker compared to the case of Au nanoparticles. Figure 3.3 shows an image of Si nanoparticles physisorbed to the gold surface in an aqueous suspension. At power levels of 4.4 $\mu W/\mu m^2$, the particles are clearly seen. Panel 3.3 b) shows the logarithm of the fluorescence signal in the indicated region of interest, showing well resolved spots . Panel 3.3 (c) depicts the corresponding transmission image, obtained by illuminating the sample with a halogen lamp and detecting the image plane with the same camera. Comparison between the transmission and fluorescence image reveals that whereas the

brighter clusters can be seen in the transmission image, the fluorescence image identifies structures that remain invisible in transmission contrast (see encircled area). Although smaller (< 10 nm) silicon nanoparticles and porous silicon are known to exhibit strong luminescent properties of their own(Cullis and Canham, 1991; Wilson, Szajowski, and Brus, 1993; Dubertret et al., 2002), the fluorescence from 30 nm sized Si nanoparticles is rather weak. Indeed, we did not observe any fluorescence from the Si particles when dispersed on plain glass coverslips in total internal reflection fluorescence mode under similar excitation conditions, underlining that the signal is only observed when the gold film is present. We note that the fluorescence signal is stable and does not show blinking effects characteristic of semi-conducting quantum dots.

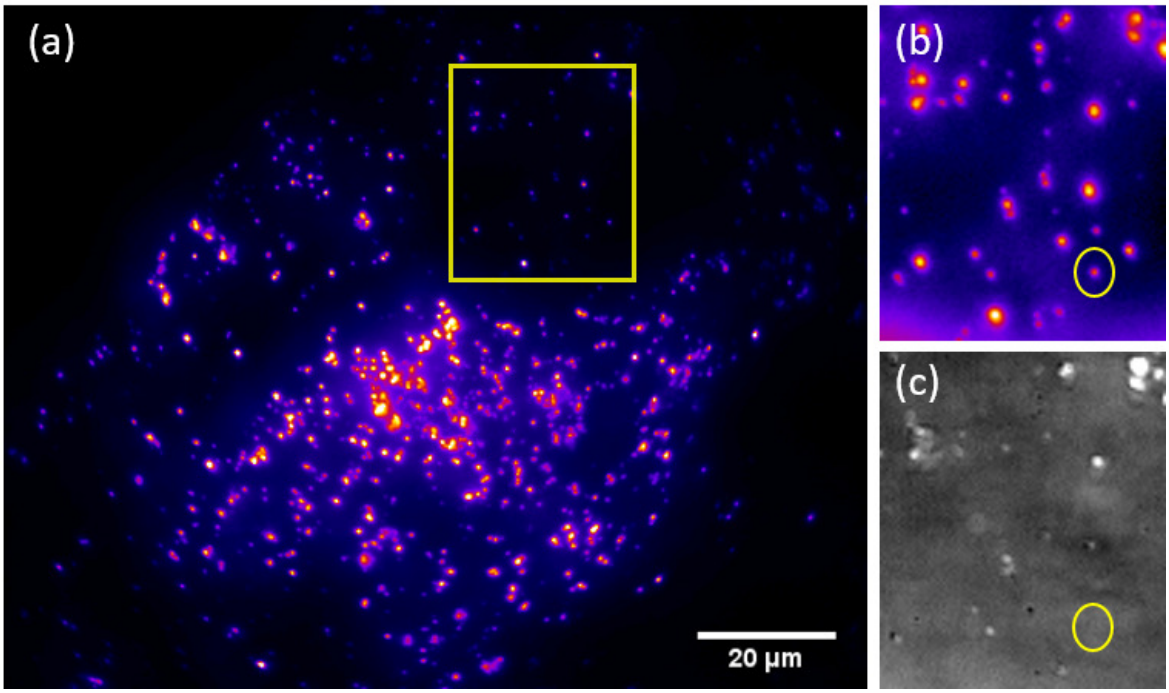

FIGURE 3.3: (a) Sensor image of 30 nm Si nanoparticles in water under illumination of $4.4\mu W/\mu m^2$. (b) Zoom of the region of interest indicated in (a). The logarithm of the signal is taken to reveal weaker emitters. (c) Transmission image of the same region of interest as in (b).

There remains the possibility that some of the bright spots observed in the signal correspond to defects in the film instead of Si particles. One method of determining the origin of the emission is to image the bare surface before introducing sample particles. The challenges in doing so is that hotspots can be very sensitive to adjustments in coupling angle, focus, and other variables that may have to be adjusted to optimize signal from particles. Meticulously monitoring of the bare film certainly complicates the usability of the sensor device. A more appealing option is to minimize the number of surface defects. One method of doing so is to use freshly cleaved mica surfaces as a substrate for the gold film. An image obtained with a

mica coverslip are shown in Fig. 3.4. Clear signals are obtained with $\sim$6.9 μW/μm^2 incident before the objective with a sparse set of hotspots prior to the addition of particles. The film is not mechanically robust however compared to a BK7 substrate. The mica films are easily bent and are permeated by water after a few hours of use. In future attempts with mica, the addition of a dielectric layer to the gold coating may produce more water resistant films.

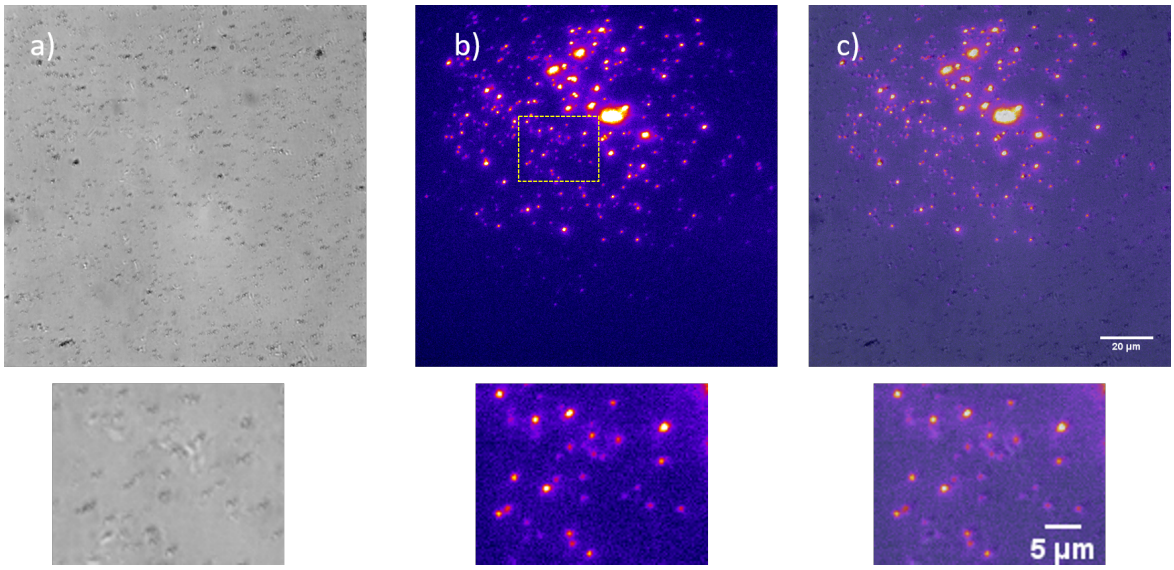

FIGURE 3.4: a) Transmission image of Si particles adhered to a 30nm Au film wiht a mica substrate. b) Signal image obtained with 100mW incident before the objective and 1 second exposures. c) An overlay of a) and b)

Another observation is the occasional appearance of interference effects which bare resemblance to artifacts seen in SPRI. The high powers used in the microscope present a challenge in filtering out excitation fields from the final image. Fig. 3.5 shows examples of how filter sets must be carefully chosen to minimize diffraction patterns. In panel a) a band pass filter centered around 540nm is placed before

the camera, resulting in no interference patterns as expected for a fluorescence signal. As the band pass approaches the incident wavelength of 800nm (716/43nm), streaking patterns become visible. Presumably, the broadband femtosecond source may have spectral tails that are able to escape filtering by the dichroic and band-pass filters resulting in interference in the far field. It is critical to limit the effects of these tails by using a long wave pass in the excitation path. This can be done with a thick glass 780 long pass filter. When the cleanup filter is removed, the interference effects become extreme as can be seen in panel c).

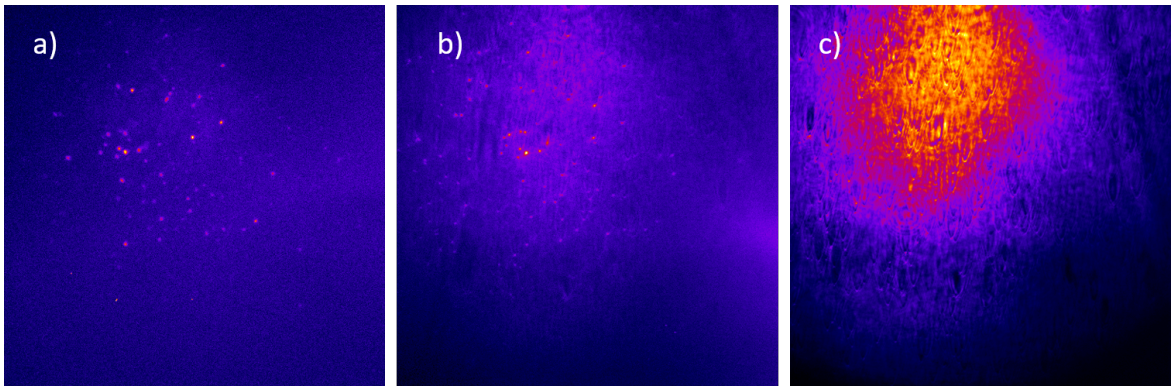

FIGURE 3.5: a) Signal image with a 540nm band pass in the emission path. b) Signal image with a 716nm band pass. c) Signal image without 780nm long pass filter in the excitation path

3.3.3 Detection of polymer particles and organic matter

Gold and silicon nanoparticles have relatively high dielectric constants, translating in strong refractive properties even when suspended in water. It is more challenging to detect objects with a refractive index closer to that of water. We perform measurements with cholesteryl oleate droplets in an aqueous medium, shown in Fig.

3.4 using $\sim$2.4 μW/μm^2 over an $\sim$70μm x 70μm field of view. Again, fluorescence signals are observed against a low background. The strength of the fluorescence signal can vary from film to film at similar illumination intensities, potentially due to inconsistent film quality.

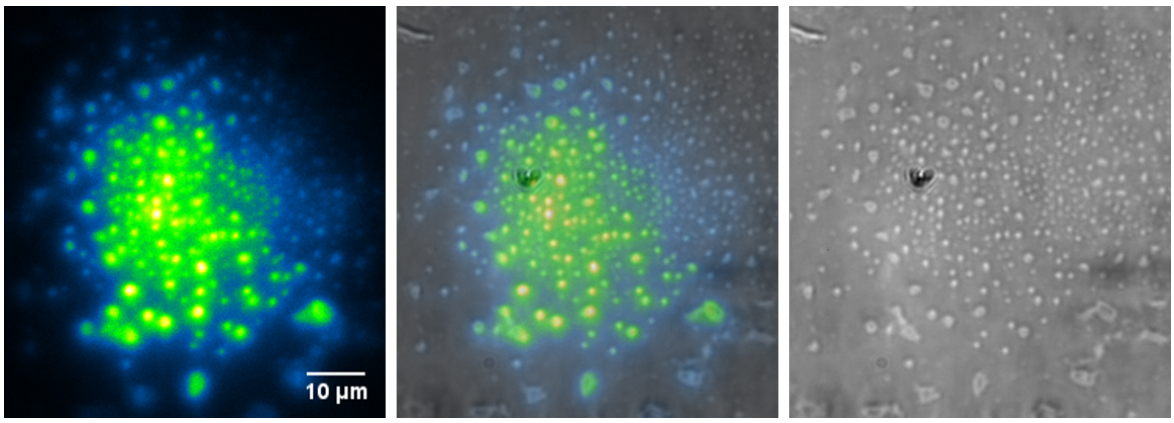

FIGURE 3.6: Cholesteryl oleate droplets adhered to the sensor surface.

We utilize polystyrene beads (350 nm) as another example of a non-fluorescent sample with a relatively low refractive index ($n \approx 1.60$). Figure 3.5 shows a two-photon excited fluorescence image of polystyrene beads adhered to the sensor surface obtained when using 150 mW of average illumination power before the objective with 1 second exposures accumulated over 20 frames ($\sim$ 10 μW/μm^2). Beads are more readily recognized in the transmission image and reveal that the signal from beads is accompanied by signal from film defects which can be brighter than the beads themselves. With lower signal to noise ratios than signals from gold particles or silicon, images more noticeably suffer from nonuniform excitation as some areas of the film do not yield a clear signal from visibly adhered beads. The power needed to generate these images are near the damage threshold for typical 30 nm gold films

(∼200 mW for a femtosecond source), and the weak signal that results suggests that this sample is near the current limits of the sensors detection abilities.

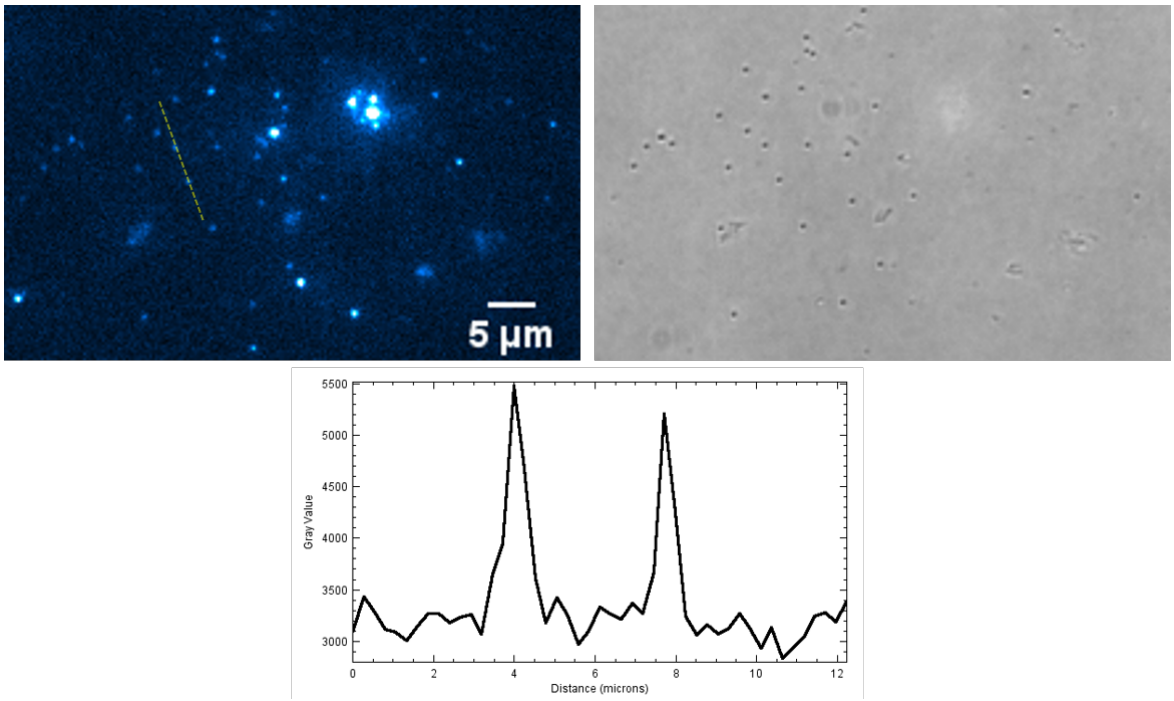

FIGURE 3.7: (a) Polystyrene beads (350 nm) suspended in water.

Fig. 3.8 shows another image of polystyrene beads. The brighter regions of the image correspond to clusters of particles while dimmer spots largely correspond to individual beads in the transmission image. Curiously, the power needed to clearly illuminate the sample was $\sim 5.2\ \mu W/\mu m^2$, nearly half of what was used in the previous PS image. The images obtained with this specific batch of coverslips display common features that are not always observed with other gold films. A patchy background luminescence is more prominent than in other films and is more noticeable in the center region of the film. A number of low intensity bright spots that do not correspond to beads in the transmission image is also observed. One

difference with this particular batch of coverslips is the cleaning procedure used for the glass substrates as a sulfuric acid based cleaning detergent was used prior to deposition. Further experiments are required to determine how different cleaning methods effect the efficiency of signal generation and how they translate to the surface properties of the gold layer.

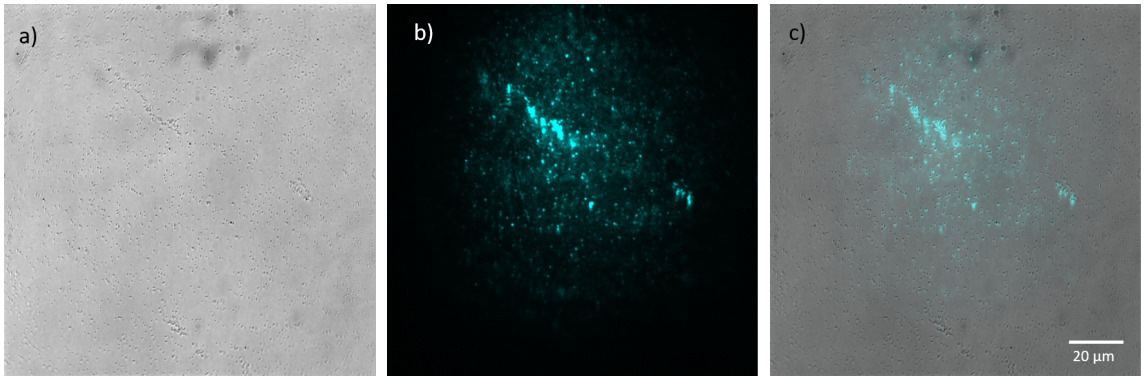

FIGURE 3.8: (a) Polystyrene beads (350 nm) suspended in water illuminated with 5.2 $\mu W/\mu m^2$

The organic material present in cells is known to have an autoflorescence that is not present in lipid droplets. In Fig. 3.9 cancer cells produce a clear image of the bottom surface of the cell adhered to the coverslip. Previous studies have shown that the enhanced evanescent SPP fields driven by femtosecond pulses are capable of driving a two photon process in the cells themselves which is not observed in TIR systems(He et al., 2009). This process is expected to contribute to the observed image here as well, though this process does not explain the signals observed in lipid droplets which are not autofluorescent. A general feature of this sensor is that samples immersed in air produce stronger signals compared to water. In the case of cancer cells, three times the incident power was needed to generate a comparable

image in water. This may be expected as an air environment offers greater contrast in index of refraction between the sample and its surroundings, however biological applications generally require an aqueous environment.

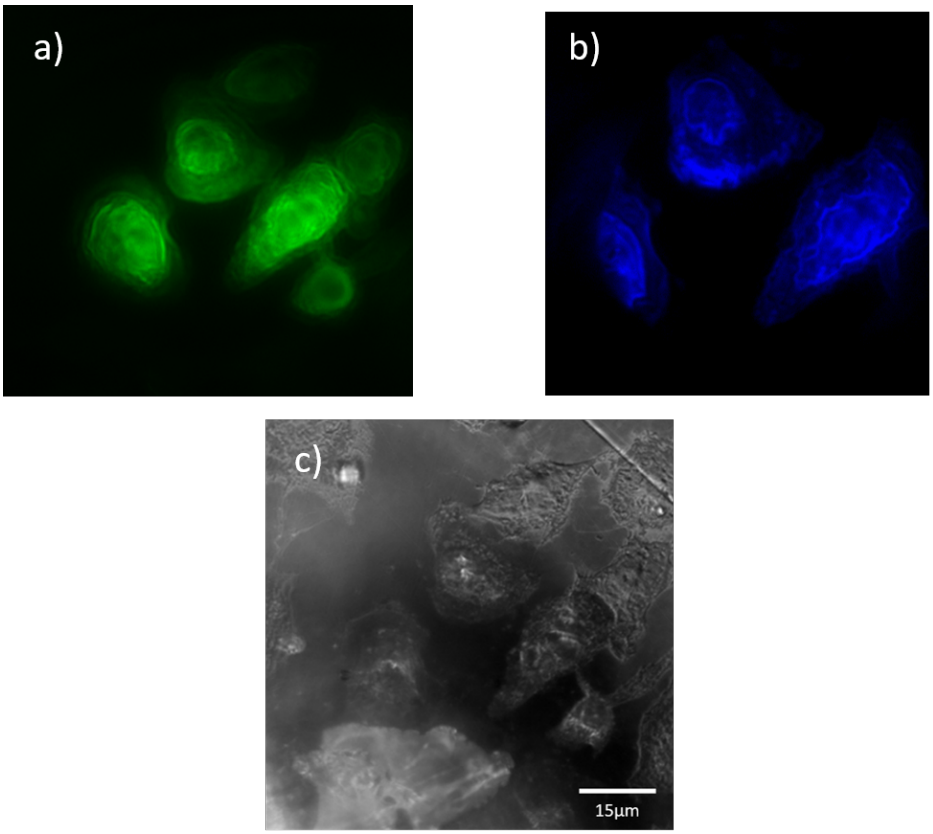

FIGURE 3.9: MCF-7 cancer cells fixed to the surface of the sensor. Cells fixed in air a). Cells in water using 1.6x telescope relative to the transmission image b). Transmission image c)

Figure 3.10 shows the dependence of the signal generated at the locations of the cholesteryl oleate droplets as the illumination power is increased. We find a power dependence close to 2, suggesting that the process responsible for the signal is indeed a two-photon excited fluorescence process. Since both polystyrene and

cholesteryl oleate are non-fluorescent, the origin of the signal is not likely the particles themselves. Rather, the experiments suggest that two-photon excited fluorescence originates from the gold sensor surface itself.

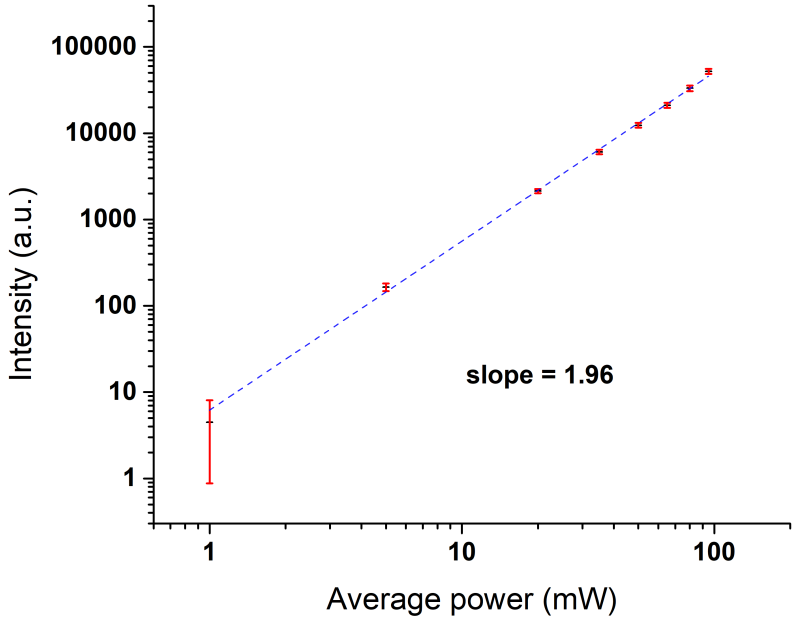

FIGURE 3.10: Magnitude of the fluorescence signal obtained from the locations of cholesteryl oleate droplets as the average power of the illuminating beam is increased. Power is measured at the back aperture of the objective lens.

3.3.4 DNA binding

One potential application for Cofefe is the detection of binding events of single strands of DNA (30A) functionalized to the sensor surface with their complementary strands (30T) bound to gold nanoparticles (40 nm Au spheres, 100 pM concentration) in solution. Real time SPRI measurements apply ~1 mW to a comparable field of view and typically apply a time differencing scheme such that only diffraction patterns associated with binding events within the last exposure are displayed in a given frame. Binding events can be clearly observed in the Cofefe microscope with 25mW incident on the film and display a symmetric spot at the location of the event that is registered continuously in time. The frames below represent time steps of two minutes.

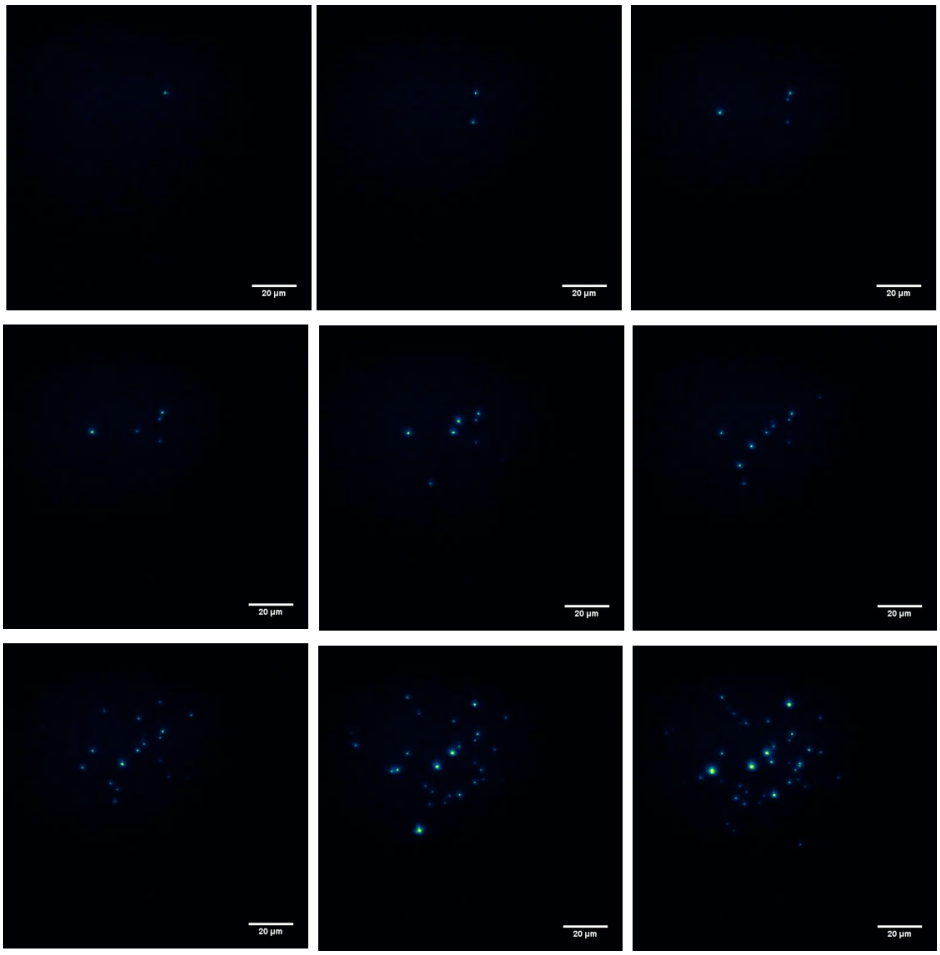

FIGURE 3.11: Binding events in time. Each frame represents a time interval of two minutes

The emission patterns display an intensity that varies in time and has a strong dependence on the incident intensity. A representative sample of intensity plots of individual binding events as a function of time are shown in Fig. 3.12. At 25mW incident before the objective, binding events appear as a bright flash that quickly decays and then slowly increases again before settling to an equilibrium value at timescales on the order of minutes. With 90 mW, the bright flash quickly decays

to an equilibrium value without an intermediate increase in intensity, displayed in Fig. 3.12. One consideration in this behavior is the heat produced locally at the surface, which could be markedly different at the two powers used. Aside from potential morphological changes, emission spectra from gold nanoparticles have been shown to be sensitive to heating effects. Red shifting of plasmon resonances with increasing temperature have been observed by others, and raises the question of how the overall Cofefe signal may vary with time and temperature through a fixed set of detection filters .Honda et al., 2011

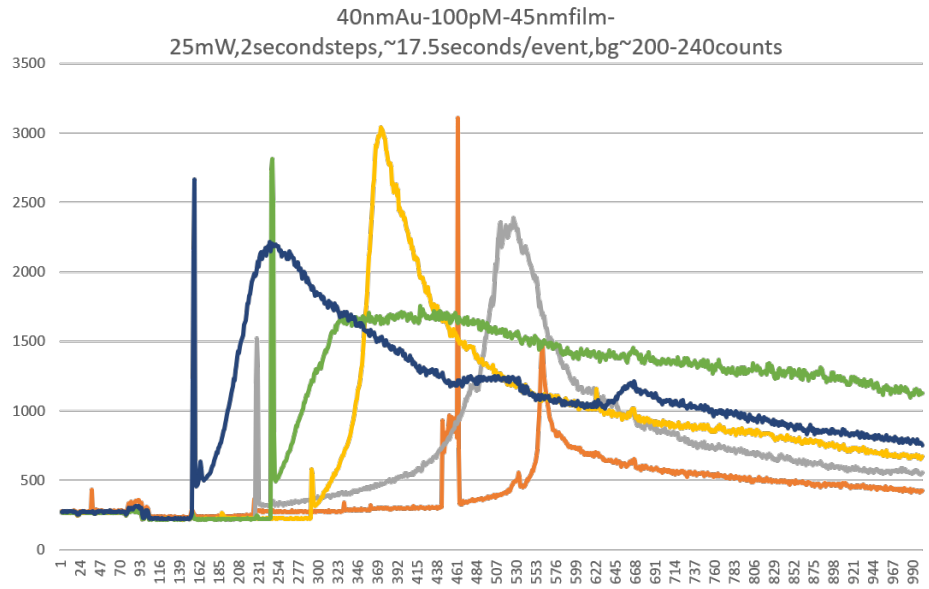

FIGURE 3.12: Plot of intensity from typical binding events with 25 mW incident on the sample

Heat induced convection currents have been observed in the sample solution and effect the observed binding rates which occur at much longer time intervals than in SPRI with similar particle concentrations. The low powers used in SPRI produce

small enough heating effects that binding rates may be attributed to the diffusion of particles through solution. In contrast, binding rates in Cofefe show a great deal of variability and occasionally results in little to no observations of binding events. Successful development of this application will require additional control and modeling of the fluid flow at the surface. The incorporation of a flow cell to the sensor surface is one potential method of mitigating heating effects. A laminar flow of analytes over the surface would provide a clearer dependence of binding rates on particle concentration.

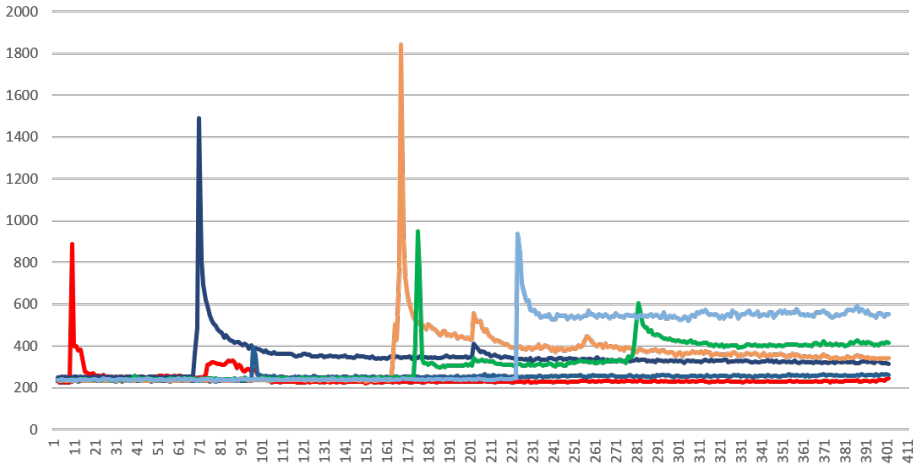

FIGURE 3.13: Plot of intensity of typical binding events with 90 mW incident on the sample

3.3.5 SRRF

For a sparse set of isolated emitters fitting methods can estimate fluorophore position with a single frame with high precision. For imaging applications, high spatial resolution requires a dense labeling of the sample with fluorophores which also

results in a much more convoluted and often intractable fitting procedure. The multiplexing ability of optical detectors is similarly limited by the ability to spatially resolve the emission from neighboring emitters in a short period of time. A fully utilized multiplexed sensor should not only be able to localize a signal spatially but have the ability to simultaneously detect adjacent events just outside of the spatial resolution limit, yielding maximum throughput. To enhance this ability in the Cofefe microscope, improvements in spatial accuracy must be accompanied by the ability to register events with high spatial density. The incoherent radially symmetric emission pattern observed in Cofefe lends itself to existing fluorescence methods for improving spatial resolution.

Super resolution methods generally rely on the ability of a series of low resolution images to implicitly carry higher frequency information than is present in any individual low resolution frame. Super resolution methods such as PALM and STORM rely on the intermittent emission of fluorophores to localize spatial features, but the effective fluorophore in Cofefe is a spatially localized region of the gold film which radiates continuously. The Cofefe signal from nearby emitters is analogous to the high emitter density limit in conventional fluorescence microscopy, where the high density of emitters limits the ability to resolve blinking statistics from a large background. SRRF has shown the ability to improve spatial resolution in this high density limit across a wide range of data sets by analyzing the intensity gradient fields of a series of wide field images. Assuming that the signal represents a collection of point emitters with a radially symmetric point spread function, SRRF can detect regions of higher local radial symmetry than their surroundings.(Gustafsson et al., 2016) By correlating radial symmetry maps from a sequence of raw frames,

in time, SRRF provides a rapid evaluation of likely emitter positions with a single super resolution image.

The strength of the Cofefe signal allows meaningful data to be collected over very short exposure times. The high frame rates achievable in EMCCD cameras, along with the short computation time needed for SRRF analysis, can be used to generate high resolution emitter mappings with high temporal resolution. A series of 100 raw wide field frames have been used in Andor's SRRF Stream camera to produce enhanced live imaging at 1fps, suggesting that live enhanced contrast sensing may be possible for gold particles in solution.(Gustafsson et al., 2016) Figure 3.10 shows a single super resolution image of 20 nm Au particles, generated from 100 raw frames acquired at 68 fps. The SRRF algorithm was run through the nanoj SRRF plugin for ImageJ. For comparison, the SRRF signal is overlayed on the raw accumulated Cofefe image acquired over the same interval of time. Isolated emitters show a reduced FWHM of $\sim$120-140 nm and increased discrimination can be seen in regions of high density, suggesting that the inherent multiplexing ability in Cofefe may be enhanced through computational methods and displayed rapidly in time.

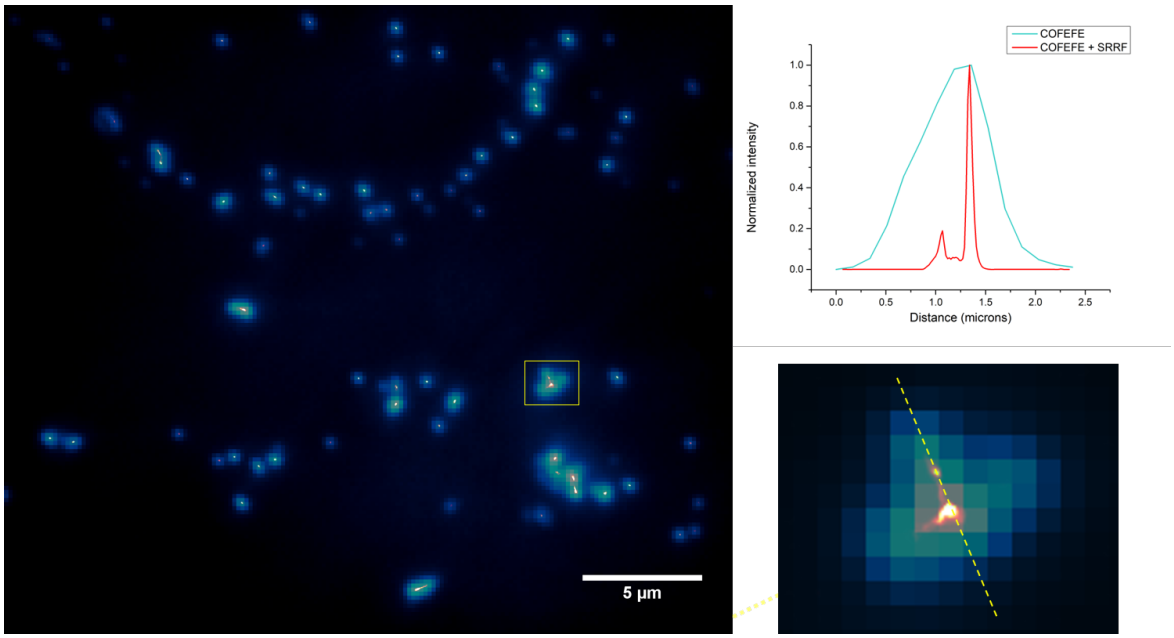

FIGURE 3.14: Overlay of Cofefe image with result after applying SRRF

3.4 Discussion

In this work, we have constructed a sensor based on the excitation of SPP modes in a thin gold film by a femtosecond laser beam. When the radiation from the film is projected onto a camera, we observe clear signals from locations where particles are in close proximity to the gold film. This radiation appears in the spectral window where we expect the two-photon excited fluorescence from gold to be prominent. The experiments described above demonstrate that this signal does not only appear for plasmonically active gold nanoparticles, but also for silicon nanoparticles, polymer beads and lipid droplets. These observations strongly suggest that the gold layer itself contributes to the detected radiation. In case of non-fluorescent particles

such as polystyrene nanospheres and lipid droplets, the gold layer is expected to be the sole origin of two-photon excited fluorescence.

It is well known that electron-hole pairs can be excited by the process of two-photon absorption in gold.Boyd, Lu, and Shen, 1986; Beversluis, Bouhelier, and Novotny, 2003 Using a near-infrared laser, electrons are excited from the d-band to the sp-band conduction band, see Fig.(a). Radiative electron-hole recombination is expected around symmetry points in the Brillouin zone where the density of states in the conduction band is high. Such a condition is found near the Fermi level of the X and L symmetry points, which correspond to radiative energies of 1.8 eV and 2.4 eV, respectively, upon recombination of momentum-matched electrons in the conduction band and holes in the valence band. In case of confined and enhanced local fields near the gold surface, both the absorption and emission rates are expected to increase, producing efficient two-photon excited fluorescence from gold.Boyd, Lu, and Shen, 1986; Beversluis, Bouhelier, and Novotny, 2003 The formation of nano-cavities can furthermore relax the photon-momenta, enabling transitions in a broader region near the X and L symmetry points and resulting in a spectrally broadened emission.

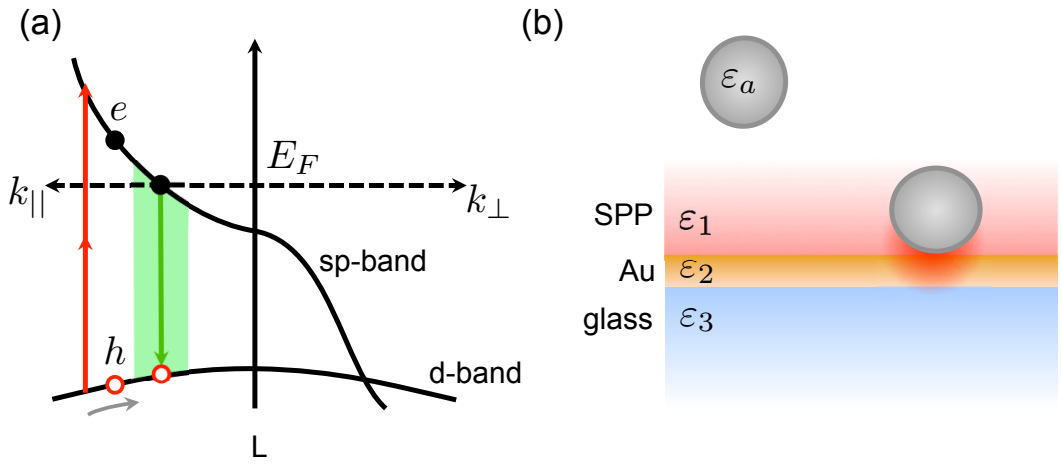

FIGURE 3.15: (a) Band structure of gold and the proposed electron-hole pair generation induced by two-photon absorption (red arrows), followed by radiative recombination (green shaded area). Dashed line denotes the Fermi level. (b) Proposed mechanism of the sensor. A particle of dielectric constant ε_a moves in an aqueous solution of dielectric constant ε_1. Upon illumination through the glass medium (ε_3), SPP modes are excited at the gold/liquid interface. Adsorption of the particle to the gold surface produces confined fields near the binding site, inducing two-photon absorption in the gold layer. Radiative electron-hole recombination is facilitated by the field confinement and the antenna properties of the gold film.

Our results confirm that the two-photon excited fluorescence of the bare smooth gold is very inefficient.(Beversluis, Bouhelier, and Novotny, 2003) Under SPP illumination conditions, the gold film itself produces a negligible amount of emission which is near the noise floor of our camera. However, whenever a nanoparticle is in the vicinity of the film, fluorescence emission is observed. This observation suggests that the confinement of the field between the gold and the particle yields local fields sufficient for two-photon excitation of electron-hole pairs in the gold, as schematically depicted in Fig. (b). This process is evidently efficient if the nanoparticle is gold, giving rise to strongly enhanced fields, but our experiments show that

polymer particles or lipid droplets yield confined fields that are also capable of triggering two-photon absorption.

The subsequent emission process is furthermore enhanced by the gold film. The emission pattern observed in the back focal plane shows that the majority of the radiation couples out at the Kretschmann angle, indicating that the local polarization near the particle excites surface plasmon polaritons in the film, which subsequently couple to the far field as leakage radiation. (Gryczynski et al., 2005; Kenison et al., 2017) This latter mechanism is similar to the enhanced emission seen in SPCE microscopy. (Lakowicz et al., 2003; Gryczynski et al., 2004; Stefani et al., 2005; Borejdo et al., 2006; He et al., 2009; Lin et al., 2010; Cao et al., 2012) Previous work in SPCE microscopy has shown the utility of confined local fields to boost the optical signal generated at the gold/sample interface.(Cao et al., 2014; Cao et al., 2017) Our work extends some of the principles developed for SPCE microscopy to include signal generation in the absence of fluorophores, thus constituting a completely label-free approach. In our sensor, the gold film plays a dual role: it is the site of the optical excitation and it acts as an antenna to couple the local polarization in the form of radiation to the far-field.

The mechanism described above is consistent with our observations. We will call this mechanism confined optical field enhanced fluorescence emission, or Cofefe. The Cofefe sensor enables detection of non-fluorescent particles that physisorb to the gold sensor surface. In its current version, the sensor largely reproduces the capabilities of SPRM. However, the detected signal in Cofefe appears relative to a dark background and the detected spot exhibits a pointspread function that is based

on incoherent emission and thus does not display interferences among different detected spots. In addition, the performance of the device can be improved, for instance by optimizing the pulse parameters, detection filters and quality of the gold sensing surface.

3.5 Conclusion

We have constructed a sensor that enables the detection of particles near a gold sensing surface. The optical signal is based on the two-photon excited fluorescence from the gold, enabled by the formation of confined optical fields upon binding/adsorption of the particle to the substrate. We have shown that this sensor, called Cofefe, is capable of registering non-fluorescent particles through the process of gold fluorescence. Unlike SPR-based sensors, the Cofefe method produces background-free signals and yields non-interfering and highly confined spots on the camera detector. These attributes make the Cofefe sensor an attractive candidate for label-free binding and sensing studies.

Bibliography

Axelrod, Daniel (1981). "Cell-substrate Contacts Illuminated by Total-Internal Reflection Fluorescence". In: *Journal of Cell Biology* 89.9, pp. 141–145.

Beversluis, Michael, Alexandre Bouhelier, and Lukas Novotny (2003). "Continuum generation from single gold nanostructures through near-field mediated intraband transitions". In: *Physical Review B - Condensed Matter and Materials Physics* 68.11, pp. 1–10.

Bharadwaj, Palash, Alexandre Bouhelier, and Lukas Novotny (2011). "Electrical excitation of surface plasmons". In: *Physical Review Letters* 106.22, pp. 1–4.

Boozer, Christina et al. (2006). "Looking towards label-free biomolecular interaction analysis in a high-throughput format: a review of new surface plasmon resonance technologies". In: *Curr. Opin. Biotechnol.* 17.4, pp. 400–405.

Borejdo, J et al. (2006). "Fluorescence correlation spectroscopy in surface plasmon coupled emission microscope". In: *Opt. Express* 14.17, pp. 7878–7888.

Boyd, G T, Z H Lu, and Y R Shen (1986). "Photoinduced luminescence from the noble metals and its enhancement on roughened surfaces". In: *Phys. Rev. B* 33, pp. 7923–7936.

Brockman, Jennifer M, Bryce P Nelson, and Robert M Corn (2000). "Surface plasmon resonance imaging measurements of ultrathin organic films". In: *Annual review of physical chemistry* 51.1, pp. 41–63.

Cao, S et al. (2012). "Surface plasmon-coupled emission: what can directional fluorescence bring to the analytical sciences?" In: *Annu. Rev. Phys. Chem.* 5, pp. 317–336.

Cao, S H et al. (2014). "Label-free aptasensor based on ultrathin-linker-mediated hot-spot assembly to induce strong directional fluorescence". In: *J. Am. Chem. Soc.* 136.(19), pp. 6802–6805.

Cao, S.-H. et al. (2017). "Surface Plasmon-Coupled Emission". In: *Surface Plasmon Enhanced, Coupled and Controlled Fluorescence*. Ed. by C D Geddes. John & Sons: Wiley.

Chiu, Kuo-Chih et al. (2011). "Optimizing silver film for surface plasmon-coupled emission induced two-photon excited fluorescence imaging". In: *Optics Express* 19.6, p. 5386.

Cullis, A G and L T Canham (1991). "Visible light emission due to quantum size effects in highly porous crystalline silicon". In: *Nature* 353, pp. 335–338.

Doremus, Robert H. (1964). "Optical properties of small gold particles". In: *The Journal of Chemical Physics* 40.8, pp. 2389–2396.

Drezet, A. et al. (2008). "Leakage radiation microscopy of surface plasmon polaritons". In: *Materials Science and Engineering B: Solid-State Materials for Advanced Technology* 149.3, pp. 220–229.

Dubertret, B et al. (2002). ""In vivo imaging of quantum dots encapsulated in phospholipid micelles,"" in: *Science* 298, pp. 1759–1762.

Fast, Alexander et al. (2016). “Surface-enhanced coherent anti-Stokes Raman imaging of lipids”. In: *Appl. Opt.* 55.22, pp. 5994–6000.

Fontana, Eduardo (2006). “Thickness optimization of metal films for the development of surface-plasmon-based sensors for nonabsorbing media”. In: *Applied optics* 45.29, pp. 7632–7642.

Green, R J et al. (2000). “Surface plasmon resonance analysis of dynamic biological interactions with biomaterials”. In: *Biomaterials* 21.18, pp. 1823–1835.

Gryczynski, Ignacy et al. (2004). “Surface plasmon-coupled emission with gold films”. In: *J. Phys. Chem. B* 108.33, pp. 12568–12574.

Gryczynski, Ignacy et al. (2005). “Directional two-photon induced surface plasmon-coupled emission”. In: *Thin Solid Films* 491.1, pp. 173–176.

Gustafsson, N et al. (2016). “Fast live-cell conventional fluorophore nanoscopy with ImageJ through super-resolution radial fluctuations”. In: *Nat Comm.* 7, p. 12471.

Halpern, Aaron R et al. (2014). “Single-nanoparticle near-infrared surface plasmon resonance microscopy for real-time measurements of DNA hybridization adsorption”. In: *ACS Nano* 8, pp. 1022–1030.

He, Ruei-Yu et al. (2009). “Surface plasmon-enhanced two-photon fluorescence microscopy for live cell membrane imaging”. In: *Opt. Express* 17.8, pp. 5987–5997.

Heideman, R G and P V Lambeck (1999). “Remote opto-chemical sensing with extreme sensitivity: design, fabrication and performance of a pigtailed integrated optical phase-modulated Mach–Zehnder interferometer system”. In: *Sensors and Actuators B: Chemical* 61.1-3, pp. 100–127.

Hohenau, A. et al. (2011). “Surface plasmon leakage radiation microscopy at the diffraction limit”. In: *Optics Express* 19.25, p. 25749.

Homola, J. (2008). "Surface plasmon resonance sensors for detection of chemical and biological species". In: *Chemical reviews* 108.2, pp. 462–493.

Homola, Jiří', Sinclair S Yee, and Günter Gauglitz (1999). "Surface plasmon resonance sensors". In: *Sensors and Actuators B: Chemical* 54.1-2, pp. 3–15.

Honda, Mitsuhiro et al. (2011). "Nanoscale heating of laser irradiated single gold nanoparticles in liquid". In: *Optics Express* 19.13, p. 12375.

Huang, Bo, Fang Yu, and Richard N Zare (2007). "Surface Plasmon Resonance Imaging Using a High Numerical Aperture Microscope Objective". In: *Anal. Chem.* 79.7, pp. 2979–2983.

Johnson, P. B. and R. W. Christy (1972). "Optical constants of the noble metals". In: *Physical Review B* 6.12, pp. 4370–4379.

Jordan, Claire E et al. (1997). "Surface plasmon resonance imaging measurements of DNA hybridization adsorption and streptavidin/DNA multilayer formation at chemically modified gold surfaces". In: *Analytical Chemistry* 69.24, pp. 4939–4947.

Kano, Hiroshi and Wolfgang Knoll (2000). "A scanning microscope employing localized surface-plasmon-polaritons as a sensing probe". In: *Optics Communications* 182.1-3, pp. 11–15.

Kenison, J P et al. (2017). "Imaging properties of surface-enhanced coherent anti-Stokes Raman scattering microscopy on thin gold films". In: *J. Opt Soc. Am. B* 34.(10), pp. 2104–2114.

Kooyman, R P H et al. (1988). "Surface plasmon resonance immunosensors: sensitivity considerations". In: *Anal. Chim. Acta* 213, pp. 35–45.

Kossoy, Anna et al. (2014). "Optical and structural properties of ultra-thin gold films". In: *Advanced Optical Materials* 3.1, pp. 71–77.

Kreibig, U. (1977). "Anomalous Frequency and Temperature Dependence of the Optical Absorption of Small Gold Particles". In: *J. Phys. Colloques* 38.C2, pp. 97–103.

Kuhlicke, Alexander et al. (2013). "In situ observation of plasmon tuning in a single gold nanoparticle during controlled melting". In: *Nano Letters* 13.5, pp. 2041–2046.

Kukura, Philipp et al. (2009). "High-speed nanoscopic tracking of the position and orientation of a single virus". In: *Nature methods* 6.12, p. 923.

Lakowicz, Joseph R et al. (2003). "Directional surface plasmon-coupled emission: a new method for high sensitivity detection". In: *Biochem. Biophys. Res. Commun.* 307.3, pp. 435–439.

Le Ru, E. C. et al. (2007). "Surface enhanced raman scattering enhancement factors: A comprehensive study". In: *Journal of Physical Chemistry C* 37, pp. 13794–13803.

Li, Tao et al. (2017). "Revealing the Mechanism of Photoluminescence from Single Gold Nanospheres by Defocused Imaging". In: *ACS Photonics* 8, pp. 2003–2010.

Lin, Chun-Yu et al. (2010). "Surface plasmon-enhanced and quenched two-photon excited fluorescence". In: *Opt. Express* 18.12, pp. 12807–12817.

Link, Stephan and Mostafa A. El-Sayed (1999). "Size and Temperature Dependence of the Plasmon Absorption of Colloidal Gold Nanoparticles". In: *The Journal of Physical Chemistry B* 103.21, pp. 4212–4217.

Loebich, Otto (1972). "The optical properties of gold". In: *Gold Bulletin* 5, pp. 2–10.

Maley, Adam M et al. (2017). "Characterizing single polymeric and protein nanoparticles with surface plasmon resonance imaging measurements". In: *ACS nano* 11.7, pp. 7447–7456.

Matsubara, K, S Kawata, and S Minami (1988). "A compact surface plasmon resonance sensor for measurement of water in process". In: *Applied spectroscopy* 42.8, pp. 1375–1379.

Meyer, Stefan A et al. (2012). "Combined SPR and SERS Microscopy in the Kretschmann Configuration". In: *J. Phys. Chem. A* 116.3, pp. 1000–1007.

Mooradian, A. (1969). "Photoluminescence of metals". In: *Physical Review Letters* 22.5, pp. 185–187.

Olmon, Robert L. et al. (2012). "Optical dielectric function of gold". In: *Physical Review B - Condensed Matter and Materials Physics* 86.23, pp. 1–9.

Ortega Arroyo, J et al. (2014). "Label-free, all-optical detection, imaging, and tracking of a single protein". In: *Nano letters* 14.4, pp. 2065–2070.

Ortega-Arroyo, Jaime and Philipp Kukura (2012). "Interferometric scattering microscopy (iSCAT): new frontiers in ultrafast and ultrasensitive optical microscopy". In: *Physical Chemistry Chemical Physics* 14.45, pp. 15625–15636.

Phillips, K Scott and Quan Cheng (2007). "Recent advances in surface plasmon resonance based techniques for bioanalysis". In: *Analytical and bioanalytical chemistry* 387.5, pp. 1831–1840.

Raether, H (1977). "Surface plasma oscillations and their applications". In: *Physics of Thin Films*. Ed. by G Hass, M Francombe, and R Hoffman. Academic.

Schmitt, Hans-Martin et al. (1997). "An integrated system for optical biomolecular interaction analysis". In: *Biosensors and Bioelectronics* 12.8, pp. 809–816.

Schmitt, Katrin et al. (2007). "Interferometric biosensor based on planar optical waveguide sensor chips for label-free detection of surface bound bioreactions". In: *Biosensors and Bioelectronics* 22.11, pp. 2591–2597.

Stefani, F D et al. (2005). “Surface-Plasmon-Mediated Single-Molecule Fluorescence Through a Thin Metallic Film”. In: *Phys. Rev. Lett.* 94.2, p. 23005.

Su, Yen Hsun et al. (2010). “Influence of surface plasmon resonance on the emission intermittency of photoluminescence from gold nano-sea-urchins”. In: *Nanoscale* 2.12, pp. 2639–2646.

Syal, Karan et al. (2015). “Antimicrobial susceptibility test with plasmonic imaging and tracking of single bacterial motions on nanometer scale”. In: *ACS nano* 10.1, pp. 845–852.

Wang, Shaopeng et al. (2010). “Label-free imaging, detection, and mass measurement of single viruses by surface plasmon resonance”. In: *Proceedings of the National Academy of Sciences* 107.37, pp. 16028–16032.

Wang, Yong et al. (2012). “Wide-field, surface-sensitive four-wave mixing microscopy of nanostructures”. In: *Appl. Opt.* 51, pp. 3305–3312.

Weichert, F et al. (2010). “Signal analysis and classification for surface plasmon assisted microscopy of nanoobjects”. In: *Sensors and Actuators B: Chemical* 151.1, pp. 281–290.

Wilson, W L, P F Szajowski, and L E Brus (1993). “Quantum confinement in size-selected, surface-oxidized silicon nanocrystals”. In: *Science* 262, pp. 1242–1244.

Yu, Hui et al. (2014). “Plasmonic imaging and detection of single DNA molecules”. In: *ACS nano* 8.4, pp. 3427–3433.

Yu, Hui et al. (2017). “Achieving high spatial resolution surface plasmon resonance microscopy with image reconstruction”. In: *Analytical chemistry* 89.5, pp. 2704–2707.

Yuan, C T et al. (2016). “Single fluorescent gold nanoclusters”. In: 17.18, pp. 747–749.

Zayats, Anatoly V., Igor I. Smolyaninov, and Alexei A. Maradudin (2005). "Nano-optics of surface plasmon polaritons". In: *Physics Reports* 408.3-4, pp. 131–314.

Zhang, L M and D Uttamchandani (1988). "Optical chemical sensing employing surface plasmon resonance". In: *Electronics Letters* 24.23, pp. 1469–1470.